1 # Seismic wave modeling of fluid-saturated fractured porous rock:
2 # Including fluid pressure diffusion effects of discrete distributed large-
3 # scale fractures

4 Yingkai Qi[1,2], Xuehua Chen[1,2], Qingwei Zhao[1,2], Xin Luo[1], Chunqiang Feng[3]

5 [1]State Key Laboratory of Oil & Gas Reservoir Geology and Exploitation, Chengdu University of Technology, Chengdu,
6 610059, China

7 [2]Key Laboratory of Earth Exploration & Information Techniques of Ministry of Education, Chengdu University of Technology,
8 Chengdu, 610059, China

9 [3]Exploration & Development Research Institute of Henan Oilfield, Sinopec, 473000, China

10 *Correspondence to*: Xuehua Chen (chen_xuehua@163.com)

11 **Abstract.** The scattered seismic waves of fractured porous rock are strongly affected by the wave-induced fluid pressure

12 diffusion effects between the compliant fractures and the stiffer embedding background. To include these poroelastic effects

13 in seismic modeling, we develop a numerical scheme for discrete distributed large-scale fractures embedded in fluid-saturated

14 porous rock. Using Coates and Schoenberg's local effective medium theory and Barbosa's dynamic linear slip model

15 characterized by complex-valued and frequency-dependent fracture compliances, we derive the effective viscoelastic

16 compliances in each spatial discretized cell by superimposing the compliances of the background and the fractures. The

17 effective governing equations of the fractured porous rock are then characterized by the derived anisotropic, complex-valued,

18 and frequency-dependent effective compliances. We numerically solved the effective governing equations by mixed-grid

19 stencil frequency-domain finite-difference method. The good consistency between the scattered waves off a single horizontal

20 fracture calculated using our proposed scheme and those calculated using the poroelastic linear slip model shows that our

21 modeling scheme can properly include the FPD effects. We also find that for a P-point source, the amplitudes of the scattered

22 waves from a single horizontal fracture are strongly affected by the fluid stiffening effects due to fluid pressure diffusion, while

23 for an S-point source, the scattered waves are less sensitive to fluid pressure diffusion. In the case of the conjugate fracture

24 system, the scattered waves from the bottom of the fractured reservoir and the reflected waves from the underlying formation

25 are attenuated and dispersed by the FPD effects for both P- and S-point sources. The proposed numerical modeling scheme

26 can also be used to improve migration quality and the estimation of fracture mechanical characteristics in inversion.

27 ## 1 Introduction

28 Fluid saturated porous rock in the reservoir characterized by a heterogeneous internal structure consisting of a solid skeleton

29 and interconnected fluid-filled voids, are often permeated by much more compliant and permeable fractures. Although the

30 fractures typically occupy only a small volume, they tend to dominate the overall mechanical and hydraulic properties of the

31   reservoir (Liu et al., 2000; Gale et al., 2014). Thus, fracture detection, characterization and imaging are of great importance

32   for reservoir prediction and production. Seismic waves are widely used for these purposes because their behaviors (amplitude,

33   phase and anisotropy) are strongly affected by the fractures (Chapman, 2003; Gurevich, 2003; Brajanovski et al., 2005;

34   Carcione et al., 2011; Rubino et al., 2014). Therefore, appropriate numerical modeling methods are required for the

35   interpretation, migration and inversion of seismic data from porous media containing discrete distributed fractures.

36   Biot's poroelastic theory (Biot, 1956a; b) is the fundamental theory to describe elastic wave propagation in fluid porous media,

37   including the dynamic interactions between rock and pore fluid. However, the original theory, assuming a macroscopically

38   homogeneous porous media saturated by a single fluid phase, is fail to explain the measured velocity dispersion and attenuation

39   of seismic waves (Nakagawa et al., 2007). In recent decades, many researchers found that if porous media contains mesoscale

40   heterogeneity (ignored by Boit), a local fluid-pressure gradient will be induced by the passing wave at scale comparable to the

41   wave-induced fluid pressure diffusion length (the wavelength of slow P-wave), causing significant velocity dispersion and

42   velocity attenuation at seismic frequency band (White et al., 1975; Dutta and Odé, 1979; Johnson, 2001; and Müller et al. 2008;

43   Norris, 1993; Gurevich et al., 1997; Gelinsky and Shapiro, 1997; Kudarova et al., 2016). Fractures embedded in homogeneous

44   porous background are special heterogeneities, exhibiting strong mechanical contrasts with background. When seismic waves

45   travel through fluid saturated fractured porous rocks, local fluid pressure gradients will be induced between the fractures and

46   the background in response to the strong compressibility contrast. To return the equilibrium state, fluid pressure diffusion (FPD)

47   occurs between the fractures and the embedding background, which in turn changes the fluid stiffening effect on the fractures

48   and thus their mechanical compliances depending on frequency (Barbosa et al., 2016a, b).

49   When fractures with apertures and lengths much smaller than the wavelengths are unified distributed in porous rock, the

50   properties of fractured rock are homogeneous at macroscopic scale and can be described by a representative elementary volume

51   (REV). Various effective medium theories are available for estimating the fracture-induced anisotropy, attenuation and

52   dispersion behaviors (Hudson, 1981; Thomsen, 1995; Chapman, 2003; Brajanovski et al., 2005; Krzikalla et al. 2011; Galvin

53   et al., 2015; Guo et al., 2017a; b). The discrete distributed large-scale fractures (the presence of spatial correlations of fractures),

54   however, cannot be modeled by any above-mentioned effective medium theories originally for macroscopically uniformly

55   distributed fractures. The seismic response of individual fracture is mostly assessed in the framework of the linear slip model

56   (LSM) by modeling a fracture as a nonwelded interface across which the displacement tensors are assumed to be discontinuous

57   while the stress tensors are continuous (Schoenberg, 1980). Various local numerical schemes have been developed for discrete

58   distributed large-scale fractures. The most widely used scheme is local effective-medium schemes (Coates and Schoenberg,

59   1995; Igel et al., 1997; Vlastos et al., 2003; Oelke, et al., 2013) that determine and incorporate the behavior of fracture-induced

60   media within each spatial discretized cell. The advantage of using the local effective medium is that it requires no special

61   treatment of the displacement discontinuity conditions on the fractures. An alternative scheme is the explicit interface scheme

62   that directly treat the displacement discontinuity across each fracture (Zhang, 2005; Cui et al., 2018; Khokhlov, et al., 2021).

63   The common aspect of the aforementioned numerical modeling schemes is that they are all implemented in a purely elastic

64   framework with real-valued compliances boundary and represent both the embedding background and factures as elastic solids,

65   thus the impact of FPD effects on seismic scattering can't be accounted for. A dynamic linear slip model incorporating FPD

66   effects should be considered when implementing numerical modeling of seismic wave propagating in fluid saturated porous

67   rocks containing discrete distributed large-scale fractures. Rubino et al. (2015) proposed a frequency-dependent complex-

68   valued normal compliance for regularly distributed planar fractures (a set of aligned fractures) with a separation much smaller

69   than the prevailing seismic wavelength. Despite the ability of including the FPD across the fractures, the model is not suitable

70   for modeling discrete distributed fractures. Nakagawa and Schoenberg (2007) developed an extended LSM for a single fracture

71   in the context of poroelasticity. The proposed model representing both the background and the fracture as poroelastic media

72   can appropriately incorporate the frequency related effects, but it will also result in a higher computational consuming and

73   more memory requirements. In the context of viscoelasticity, Barbosa et al. (2016a) developed a viscoelastic linear slip model

74   (VLSM) for an individual fracture with explicit complex-valued and frequency-dependent fracture compliances, to account

75   for the impact of FPD on the fracture stiffness. That provides a viscoelasticity-based modeling algorithm for discrete distributed

76   large-scale fractures with smaller computational costs and memory requirements than the poroelasticity based modeling.

77   In this paper, we develop a viscoelastic numerical modeling scheme to simulate seismic wave propagation in fluid-saturated

78   porous media containing discrete distributed large-scale fractures. To capture the FPD effects between the fractures and

79   background, we use the local effective medium theory based on Barbosa's VLSM to derive the effective anisotropic

80   viscoelastic compliances in each numerical cell by superimposing the compliances of the background and the fractures. The

81   effective anisotropic viscoelastic governing equations of the fractured porous rock are then numerically solved using mixed-

82   grid stencil frequency-domain finite-difference method (FDFD) (Hustedt, et al. 2004; Operto, et al. 2009; Liu et al., 2018). To

83   validate the proposed viscoelastic modeling scheme can capture the impact of FPD effects on seismic wave scattering, we

84   compare the scattered waves of a single horizontal fracture obtained using our proposed modeling scheme with those obtained

85   using poroelastic modeling scheme and elastic modeling scheme. Numerical examples of a fractured reservoir are presented

86   to demonstrate that the proposed modeling scheme can properly simulate the wave attenuation and dispersion due to the FPD

87   effects between the fracture system and background. A complex modified Marmousi model is also use to test the proposed

88   modeling scheme and code. The scheme can be used not only to study the impact of mechanical and hydraulic of fracture

89   properties on seismic scattering but can also to improve migration quality and the estimation of fracture mechanical

90   characteristics in inversion.

91   **2 The elastic models**

92   The two most widely used non-attenuated and non-dissipative elastic models for fractured porous media are the low- and high-

93 frequency limits elastic LSM that ignore the FPD effects between the background and the fractures. The two elastic models

94 can be used to determine the effective anisotropic-elastic-moduli of the fractured porous rock.

2.1 The low-frequency limits elastic linear slip models (LFLSM)

96 The presence of fractures in a homogeneous and isotropic porous rock results in an effective anisotropic medium. The effective

97 compliance matrix of the dry fractured rock $\mathbf{S}^{dry}$ can be obtained using the LSM (Schoenberg and Sayers, 1995):

98 $$\mathbf{S}^{dry} = \mathbf{S}_b^{dry} + \mathbf{Z}_0, \tag{1}$$

99 where $\mathbf{S}_b^{dry}$ is the isotropic compliance matrix of the dry background medium in the absent of fractures, and $\mathbf{Z}_0$ is the excess

100 compliance matrix due to the dry fractures. For a single set of rotationally invariant fractures, $\mathbf{Z}_0$ can be written as

101 (Schoenberg and Sayers, 1995):

102 $$Z_{ij,0} = \frac{Z_T}{4}\left(\delta_{ik}n_l n_j + \delta_{jk}n_l n_i + \delta_{il}n_k n_j + \delta_{jl}n_k n_i\right) + \left(Z_{N_d} - Z_T\right)n_i n_j n_k n_l, \tag{2}$$

103 where n_i is the component of the local unit normal to the fracture surface, Z_{N_d} and Z_T are the drained normal fracture

104 compliance and tangential fracture compliance, respectively, as functions of fracture thickness h^c and the drained

105 longitudinal modulus H_d^c and shear moduli μ^c of the fracture (Brajanovski et al., 2005):

106 $$Z_{N_d} \equiv \frac{h^c}{H_d^c}, \quad Z_T \equiv \frac{h^c}{\mu^c}. \tag{3}$$

107 Since the fluid pressure is uniform in the low-frequency limit, the corresponding effective stiffness matrix $\mathbf{C}_{lf}^{sat}$ of the fluid

108 saturated rock can be obtained using the anisotropic Gassmann equation (Gurevich, 2003):

109 $$C_{ij,lf}^{sat} = C_{ij}^{dry} + \alpha_i \alpha_j M_{dry}, \quad i,j = 1,\dots,6. \tag{4}$$

110 The anisotropic Biot-Willis coefficients α_m are:

111 $$\alpha_m = 1 - \frac{\sum_{n=1}^{3} C_{mn}^{dry}}{3K_g}, \quad m = 1,2,3, \tag{5}$$

112 $\alpha_4 = \alpha_5 = \alpha_6 = 0$. The Biot's fluid-storage modulus M is

113 $$M_{dry} = \frac{K_g}{(1 - K_0^*/K_g) - \phi(1 - K_g/K_f)}, \tag{6}$$

114 where K_g denotes the grain solid bulk modulus, K_f the pore fluid bulk modulus, and K_0^* the generalized drained bulk

115 modulus, defined as

116 $$K_0^* = \frac{1}{9}\sum_{i=1}^{3}\sum_{j=1}^{3} C_{ij}^{dry}. \tag{7}$$

2.2 The high-frequency limits elastic linear slip models (HFLSM)

118 In the high-frequency limit, the fractures are hydraulically isolated from the saturated background medium. The effective

119 compliance matrix of the saturated background medium permeated by the dry fractures can be expressed as (Guo et al., 2016):

120 $$\mathbf{S}_{hf}^1 = \mathbf{S}_b^{sat} + \mathbf{Z}_0, \tag{8}$$

121   where $\mathbf{S}_b^{sat}$ is the isotropic compliance matrix of the saturated background medium in the absent of fractures. The effective

122   stiffness coefficients of the saturated fractured rock can be written as:

123    $C_{ij,hf}^{\mathrm{sat}} = C_{ij,hf}^1 + \alpha_i^1 \alpha_j^1 M_1, \quad i,j = 1, \dots, 6,$ (9)

124   where α^1 and M_1 can be again calculated using Eqs. (5)-(7) but replacing the solid grains bulk modulus K_g with saturated

125   bulk modulus of the background K_m^{sat}, the overall porosity ϕ with the fracture porosity ϕ_c.

126   **3 Nakagawa's poroelastic LSM (PLSM)**

127   Nakagawa and Schoenberg (2007) presented a PLSM in the framework of poroelasticity, representing the fracture as a highly

128   compliant and porous thin layer embedded in a much stiffer and much less porous background (Barbosa et al., 2016a). Similar

129   to the classic LSM, the PLSM assumes that across a fracture surface the stress tensor is continuous while the displacement

130   tensor is discontinuous. The discontinuous displacement components for a horizonal fracture are (Nakagawa and Schoenberg,

131   2007):

132    $[u_x] = Z_T \tau_{xz},$ (10a)

133    $[u_y] = Z_T \tau_{yz},$ (10b)

134    $[u_z] = Z_{N_D}(\tau_{zz} + \alpha P_f),$ (10c)

135    $[w_z] = -\alpha Z_{N_D}\left(\tau_{zz} + \frac{1}{B}P_f\right),$ (10d)

136   where the parameter $B = \alpha M/H_u$, and the definition of drained normal fracture compliance Z_{N_D} and tangential fracture

137   compliance Z_T are the same as those in LFLEM. Since the PLSM represents both the background and the fracture as

138   poroelasticity, it is capable to describe the discontinuous displacement of the relative fluid in addition to the solid, implying

139   that it can properly handle the FPD effects between the background and the fracture. Although it is difficult to incorporate the

140   PLSM into the effective medium theory to obtain the effective moduli of the fractured porous rock, these boundary conditions

141   can be easily incorporated into poroelastic finite-difference algorithm for modeling seismic wave scattering off large-scale

142   fractures parallel to the coordinate axis. An alternative wavenumber domain method for modeling the scattered waves by

143   poroelastic fractures is presented by Nakagawa and Schoenberg (2007) based on the PLSM.

144   **4 Barbosa's viscoelastic LSM (VLSM)**

145   Barbosa et al. (2016a) derived a VLSM that account for the FPD effects between a fracture and background and the resulting

146   stiffening effect impact on the fracture. The background is assumed to be not impacted by the FPD and can be represented by

147   an elastic solid, whose properties are computed according to Gassmann's equation. By representing fractures as extremely thin

148   viscoelastic layers, the poroelastic effects were incorporated into the classical LSM through complex-valued and frequency-

149   dependent compliances. These compliances characterize the mechanical properties of the fluid-saturated fracture.

150   4.1 The boundary conditions of VLSM

151   The discontinuous displacement components of the VLSM (Barbosa et al., 2016a) for a horizontal fracture are

152    $[u_x] = Z_T \tau_{xz},$ (11a)

153    $[u_y] = Z_T \tau_{yz},$ (11b)

154    $[u_z] = Z_N \tau_{zz} + Z_X \varepsilon_{xx},$ (11c)

155   where Z_N and Z_T are generalized normal and tangential compliances respectively, and Z_X is related to the coupling

156   between horizontal and vertical deformation of the fracture. The normal compliance Z_N and additional parameter Z_X are

157   complex-valued and frequency-dependent, while the tangential compliance Z_T is the same as for elastic and poroelastic

158   models. The three effective fracture parameters are given by Barbosa et al. (2016a)

159    $\eta_N = \frac{\eta_{N_D}\left[\alpha\eta_{N_U}D_{P_2}^b - 2B\gamma_{P_2}^b ik_{P_2}^b - 2\alpha ik_{P_2}^b\left(1/\gamma_{P_2}^b + 2B\right)\right]}{\alpha\eta_{N_D}D_{P_2}^b - 2B\gamma_{P_2}^b ik_{P_2}^b},$ (12a)

160    $\eta_X = \frac{-4k_{P_2}^b\alpha^b\eta_T M^b\mu^b\mu\left(\alpha H_U^b M - \alpha^b H_U M^b\right)}{\left(H_U^b\right)^2\left(hH_U\omega\eta_f^b + 2k_{P_2}^b MH_D\kappa^b\right)}.$ (12b)

161   We rewrite Eqs. (12a)-(12b) as

162    $Z_N = Z_{N_U} + Z_{N_D}\frac{G_1(1+i)}{\sqrt{\omega} + G_2(1+i)},$ (13a)

163    $Z_X = -\frac{G_3(1+i)}{\sqrt{\omega} + G_4(1+i)},$ (13b)

164   where Z_{N_U} and Z_{N_D} are the undrained and drained normal fracture compliance respectively, ω is the angular frequency.

165   The four real-valued parameters G_1, G_2, G_3 and G_4 are defined as

166    $G_1 = \sqrt{\frac{\kappa^b}{\eta N^b}}\frac{(B^b - B^c)^2}{\eta_{N_D}}, \qquad G_2 \approx \sqrt{\frac{\kappa^b}{\eta N^b}}\frac{1}{\eta_{N_D}},$ (14a)

167    $G_3 = \frac{2\sqrt{2}\,\alpha^b\mu^b(B^b - B^c)\sqrt{D^b}}{H_D^b}, \qquad G_4 = \frac{\sqrt{2}\,\kappa^b}{h^c\kappa^c}\frac{D^c}{\sqrt{D^b}},$ (14b)

168   where the parameters with superscripts b correspond to background properties and the parameters with superscripts c

169   correspond to fracture parameters. In Eqs. (14a)-(14b), D is the diffusivity defined as $D = \kappa N/\eta$ ($N = H_D M/H_U$), and the

170   dimensionless parameter B defined as $B = \alpha M/H_U$. H_U, H_D and μ are the corresponding undrained P wave modulus,

171   drained P wave modulus and shear modulus. The Barbosa's VLSM can properly capture the FPD effects between a fracture

172   and background.

173   4.2 The effective viscoelastic-anisotropic stiffness matrix based on Barbosa's VLSM

174   To incorporate the VLSM into viscoelastic finite-difference modeling algorithms, we give the specific derivation of the

175   effective viscoelastic-anisotropic stiffness matrix of the numerical grids on a fracture based on Coates and Schoenberg's local

176   effective medium theory (1995). The porous background is assumed to be unaffected by the FPD in the presence of fractures

177   because of the small amount of diffusing fluid and large compliance contrast between background and fluid. Thus, the rock

178   background can be represented by an elastic homogeneous solid and the strain $\boldsymbol{\varepsilon}^b$ of the background can be expressed as

179      $\varepsilon_{ij}^{b} = s_{ijkl}^{b}\sigma_{kl},$ (15)

180   where the compliance tensor $\mathbf{s}^{b}$ are computed according to Gassmann's equation (Rubino et al., 2015; Barbosa et al., 2016a),

181   and $\boldsymbol{\sigma}$ is the average stress tensor. The exceed strain tensor $\boldsymbol{\varepsilon}^{c}$ induced by a single fracture with surface S in a representative

182   volume V (e.g. the volume of numerical cell) is given by (Hudson and Knopoff, 1989; Sayers and Kachanov, 1995; Liu, et

183   al., 2000)

184      $\varepsilon_{ij}^{c} = s_{ijkl}^{c}\sigma_{kl} = \frac{1}{2V}\int([u_i]n_j + [u_j]n_i)dS,$ (16)

185   where $\mathbf{s}^{c}$ is the extra compliance tensor resulting from the fractures, $[u_i]$ is the ith component of the displacement

186   discontinuity on S and n_i is the ith component of the fracture normal. Note that Eq. (16) is applicable to finite, nonplanar

187   fractures in the long wavelength limit, i.e., the applied stress is assumed to be constant over the representative volume.

188   If we assume that the interface of the fracture is normal to the z-axis (fracture normal vector $\boldsymbol{n}$ is (0,0,1)), substituting Eqs.

189   (11a)-(11c) into Eq. (16), we can obtain the nonzero element of the exceed fracture strain tensor

190      $\varepsilon_{xz}^{c} = \frac{S}{V}Z_T\tau_{xz},$ (17a)

191      $\varepsilon_{yz}^{c} = \frac{S}{V}Z_T\tau_{yz},$ (17b)

192      $\varepsilon_{zz}^{c} = \frac{S}{V}(Z_N\tau_{zz} + Z_X\varepsilon_{xx}^{b}),$ (17c)

193   Then the exceed fracture strain tensor ε_{ij}^{c} and the background strain tensor ε_{ij}^{b} can be written in matrix from in Voigt notation

194      $\mathbf{e}^{b} = \mathbf{S}^{b}\boldsymbol{\sigma},$ (18)

195      $\mathbf{e}^{c} = \frac{S}{V}(\mathbf{Z}_1\boldsymbol{\sigma} + \mathbf{Z}_2\mathbf{e}^{b}) = \frac{S}{V}(\mathbf{Z}_1 + \mathbf{Z}_2\mathbf{S}^{b})\boldsymbol{\sigma},$ (19)

196   where the strain matrix $\mathbf{e} = [\varepsilon_{11}, \varepsilon_{22}, \varepsilon_{33}, 2\varepsilon_{23}, 2\varepsilon_{13}, 2\varepsilon_{13}]^{T}$, and the stress matrix $\boldsymbol{\sigma} = [\sigma_{11}, \sigma_{22}, \sigma_{33}, \sigma_{23}, \sigma_{13}, \sigma_{12}]^{T}$. The

197   6×6 fracture compliance matrix $\mathbf{Z}_1$ and additional dimensionless matrix $\mathbf{Z}_2$ according to the Voigt notation are defined as

198      $\mathbf{Z}_1 = \begin{bmatrix} 0 & 0 & 0 & 0 & 0 & 0 \\ 0 & 0 & 0 & 0 & 0 & 0 \\ 0 & 0 & Z_N & 0 & 0 & 0 \\ 0 & 0 & 0 & Z_T & 0 & 0 \\ 0 & 0 & 0 & 0 & Z_T & 0 \\ 0 & 0 & 0 & 0 & 0 & 0 \end{bmatrix}, \mathbf{Z}_2 = \begin{bmatrix} 0 & 0 & 0 & 0 & 0 & 0 \\ 0 & 0 & 0 & 0 & 0 & 0 \\ Z_X & 0 & 0 & 0 & 0 & 0 \\ 0 & 0 & 0 & 0 & 0 & 0 \\ 0 & 0 & 0 & 0 & 0 & 0 \\ 0 & 0 & 0 & 0 & 0 & 0 \end{bmatrix}.$ (20)

199   The average strain $\mathbf{e}$ in a homogeneous porous rock containing single fracture can be expressed as the sum of the strains of

200   background and the fractures

201      $\mathbf{e} = \mathbf{e}^{b} + \mathbf{e}^{c}.$ (21)

202   Substituting Eq. (15) and Eq. (19) into Eq. (21), we can obtain the average strain matrix

203      $\mathbf{e} = \left[\mathbf{S}^{b} + \frac{S}{V}(\mathbf{Z}_1 + \mathbf{Z}_2\mathbf{S}^{b})\right]\boldsymbol{\sigma}.$ (22)

204   Thus, the effective stiffness matrix $\mathbf{C}$ can be expressed as

205      $\mathbf{C} = \left[\mathbf{S}^{b} + \frac{S}{V}(\mathbf{Z}_1 + \mathbf{Z}_2\mathbf{S}^{b})\right]^{-1} = \mathbf{C}^{b}\left[\mathbf{I} + \frac{S}{V}(\mathbf{Z}_1\mathbf{C}^{b} + \mathbf{Z}_2)\right]^{-1}.$ (23)

206   The effective stiffness matrix of case of an inclined fracture can be obtained by rotating the coordinate axis to keep z-axis

207   perpendicular to fracture interface. We first define the inclined fracture have an angle φ and an azimuth angle θ, and then

208   the rotation matrix can be obtained:

209    $$\mathbf{R} = \begin{bmatrix} cos\theta cos\varphi & -sin\theta & cos\theta sin\varphi \\ sin\theta cos\varphi & cos\theta & sin\theta sin\varphi \\ -sin\varphi & 0 & cos\varphi \end{bmatrix},$$ (24)

210   as well as the corresponding stress Bond matrix $\mathbf{A}_\sigma$ and strain Bond matrix $\mathbf{A}_\varepsilon$. The new stress matrix $\mathbf{e}'$ and strain matrix

211    $\boldsymbol{\sigma}'$ can be expressed as the multiplication of the old one and Bond matrix

212    $$\mathbf{e}' = \mathbf{A}_\varepsilon \mathbf{e} \ , \ \boldsymbol{\sigma}' = \mathbf{A}_\sigma \boldsymbol{\sigma}.$$ (25)

213   By substituting Eq. (25) into Eq. (19), the new exceed fracture strain matrix can be obtained

214    $$\mathbf{e}^c = \frac{S}{V} \mathbf{A}_\varepsilon (\mathbf{Z}_1 + \mathbf{Z}_2 \mathbf{S}^b) \mathbf{A}_\varepsilon^T \boldsymbol{\sigma}.$$ (26)

215   Finally, substituting Eq. (6) into Eq. (21), the average strain matrix of each numerical cell containing discrete distributed

216   fractures with the same arbitrary direction can be expressed as

217    $$\mathbf{e} = \left[\mathbf{S}^b + \frac{S}{V} \mathbf{A}_\varepsilon (\mathbf{Z}_1 + \mathbf{Z}_2 \mathbf{S}^b) \mathbf{A}_\varepsilon^T \right] \boldsymbol{\sigma},$$ (27)

218   and the corresponding effective stiffness matrix $\mathbf{C}$ is

219    $$\mathbf{C} = \left[\mathbf{S}^b + \frac{S}{V} \mathbf{A}_\varepsilon (\mathbf{Z}_1 + \mathbf{Z}_2 \mathbf{S}^b) \mathbf{A}_\varepsilon^T \right]^{-1},$$ (28)

220   If the background media is isotropic, the $\mathbf{C}$ can be simplified as

221    $$\mathbf{C} = \mathbf{C}^b \left[\mathbf{I} + \frac{S}{V} \mathbf{A}_\varepsilon (\mathbf{Z}_1 \mathbf{C}^b + \mathbf{Z}_2) \mathbf{A}_\varepsilon^T \right]^{-1},$$ (29)

222   If we ignore the interaction between different fractures and the FPD along the fracture interfaces, the result can be easily

223   extended to the case of multiple sets of discrete distributed large-scale fractures with arbitrary orientation:

224    $$\mathbf{C} = \mathbf{C}^b \left[\mathbf{I} + \sum_{r=1}^{N_c} \frac{S_r}{V} \mathbf{A}_{\varepsilon r} (\mathbf{Z}_{1r} \mathbf{C}^b + \mathbf{Z}_{2r}) \mathbf{A}_{\varepsilon r}^T \right]^{-1},$$ (30)

225   where N_c is total number of the fracture directions and the subscript r denotes the rth direction. The derived effective

226   stiffness matrix is to be employed in the viscoelastic finite-difference modeling of discrete distributed large-scale fractures in

227   porous rock.

228   **5. Seismic modeling of fractured porous rock**

229   In this section, we focus on the implementation of seismic modeling of fluid-saturated porous media containing discrete

230   distributed large-scale fractures in 2D case. We develop a viscoelastic modeling scheme based on the VLSM and local effective

231   medium theory (Coates and Schoenberg, 1995) to incorporate the FPD effects between fractures and background. To validate

232   that the proposed viscoelastic modeling scheme can capture the impact of FPD effects on seismic wave scattering of fractures,

233   we outline the implementation of poroelastic modeling scheme using an explicit application of the PLSM.

5.1 viscoelastic modeling based on VLSM

For viscoelastic modeling, we adopt local effective media theory based on VLSM to derive the effective anisotropic viscoelastic compliances in each numerical cell by superimposing the compliances of the background and the fractures. Since the real structure of the rock is substituted by ideally continua, the balance equations of classical continuum mechanics can be applied without considering the discontinuity at the fracture interfaces (Lewis and Schrefler, 1998; Gavagnin et al., 2020), and the constitutive equations are characterized by effective complex-valued and frequency-dependent TTI viscoelastic stiffness. Thus, the second-order heterogeneous governing equations of fractured porous rock with PML in frequency domain can be expressed as:

$$\omega^2 \rho u_x + \frac{1}{\xi_x} \partial_x \left(\frac{c_{11}}{\xi_x} \partial_x u_x + \frac{c_{13}}{\xi_z} \partial_z u_z + \frac{c_{15}}{\xi_z} \partial_z u_x + \frac{c_{15}}{\xi_x} \partial_x u_z \right) + \frac{1}{\xi_z} \partial_z \left(\frac{c_{15}}{\xi_x} \partial_x u_x + \frac{c_{35}}{\xi_z} \partial_z u_z + \frac{c_{55}}{\xi_z} \partial_z u_x + \frac{c_{55}}{\xi_x} \partial_x u_z \right) = 0, \quad (31a)$$

$$\omega^2 \rho u_z + \frac{1}{\xi_x} \partial_x \left(\frac{c_{15}}{\xi_x} \partial_x u_x + \frac{c_{35}}{\xi_z} \partial_z u_z + \frac{c_{55}}{\xi_z} \partial_z u_x + \frac{c_{55}}{\xi_x} \partial_x u_z \right) + \frac{1}{\xi_z} \partial_z \left(\frac{c_{13}}{\xi_x} \partial_x u_x + \frac{c_{33}}{\xi_z} \partial_z u_z + \frac{c_{35}}{\xi_z} \partial_z u_x + \frac{c_{35}}{\xi_x} \partial_x u_z \right) = 0, \quad (31b)$$

where u_x and u_z are the horizontal and vertical components of particle displacement vector, ρ is the effective density, and c_{ij} are the components of complex-valued and frequency-dependent effective stiffness matrix, ξ_x and ξ_z are the frequency domain PML damping functions.

In time domain, the governing equations are integral differential equations, which require special processing for the convolution operations, resulting in high computational costs. Although the problem can be relieved (mitigated) by memory functions, it still requires high memory requirements. Instead, the governing equations can be straightforwardly solved using FDFD. To efficiently and accurately modelling of seismic wave propagation in fluid saturated fractured porous rock, we solve the second-order heterogeneous governing equations with mixed-grid stencil FDFD method (Jo et al., 1996; Hustedt et al. 2004). The mixed system of governing equations is formulated by combining the classical Cartesian coordinate system (CS) and the 45°-rotated coordinate system (RS):

$$\omega^2 \rho u_x + w_1 (A_c u_x + B_c u_z) + (1 - w_1)(A_r u_x + B_r u_z) = 0, \quad (32a)$$

$$\omega^2 \rho u_z + w_1 (C_c u_x + D_c u_z) + (1 - w_1)(C_r u_x + D_r u_z) = 0, \quad (32b)$$

where the optimal averaging coefficient $w_1 = 0.5461$ (Jo et al., 1996). The coefficients A_c, B_c, C_c, D_c and A_r, B_r, C_r, D_r are functions of the damping functions, effective stiffness coefficients and spatial derivative operators and the detailed expressions are given in Appendix A. We follow Hustedt et al., (2004) and Liu et al., (2018) to discretize the derivative operation on the mixed systems using mixed grid stencil. After discretization and arrangement, the mixed system of governing equations can be written in matrix from as

$$\begin{bmatrix} \mathbf{M} + w_1 \mathbf{A}_c + (1 - w_1) \mathbf{A}_r & w_1 \mathbf{B}_c + (1 - w_1) \mathbf{B}_r \\ w_1 \mathbf{C}_c + (1 - w_1) \mathbf{C}_r & \mathbf{M} + w_1 \mathbf{D}_c + (1 - w_1) \mathbf{D}_r \end{bmatrix} \begin{bmatrix} \mathbf{u}_x \\ \mathbf{u}_z \end{bmatrix} = \begin{bmatrix} \mathbf{0} \\ \mathbf{0} \end{bmatrix}, \quad (36)$$

where $\mathbf{M}$ denotes the diagonal mass matrix of coefficients $\omega^2 \rho$, and blocks $\mathbf{A}_c, \mathbf{B}_c, \mathbf{C}_c, \mathbf{D}_c$ and $\mathbf{A}_r, \mathbf{B}_r, \mathbf{C}_r, \mathbf{D}_r$ form the stiffness matrices for the CS and RS stencils, respectively, and the corresponding coefficients of submatrices are given in

264   Appendix B.

265   To improve the modelling accuracy of mixed-grid stencil, the acceleration term $\omega^2\rho$ are approximated using a weighted

266   average over the mixed operator stencil nodes

267     $[\omega^2\rho]_{i,j} \approx \omega^2 \left[w_{m1}\rho_{i,j} + w_{m2}(\rho_{i+1,j} + \rho_{i-1,j} + \rho_{i,j+1} + \rho_{i,j-1}) + \frac{(1-w_{m1}-4w_{m2})}{4}(\rho_{i+1,j+1} + \rho_{i-1,j-1} + \rho_{i-1,j+1} + \rho_{i+1,j-1}) \right],$ (37)

268   where the optimal coefficients $w_{m1} = 0.6248$ and $w_{m2} = 0.09381$ are computed by Jo et al. (1996).

269   In order to assess the FPD effects on seismic response, the similar procedure was adopted in the implementation of elastic

270   modeling by replacing the VLSM with the LFLSM (assuming fluid pressure is equilibrium) or the HFLSM (assuming fluid

271   pressure is unequilibrium).

272   **5.2 Poroelastic modeling based on PLSM**

273   The poroelastic modeling means that we numerically solve the Biot's equations and adopt an explicit implementation of the

274   PLSM across each fracture instead of using the effective media theory. Hence, the poroelastic modeling can naturally deal with

275   the FPD between fracture and background and account for its impact on wave scattering. Although it is difficult to implement

276   an explicit application of PLSM for arbitrary orientated fracture, it is relatively straightforward for horizontal or vertical fracture.

277   In frequency domain, the governing equations for an isotropic poroelastic media in the absent of fractures can be written as

278   (Biot, 1962):

279     $\omega^2\rho\mathbf{u} + \omega^2\rho_f\mathbf{w} + \nabla\cdot\boldsymbol{\sigma} = 0,$ (38a)

280     $\omega^2\rho_f\mathbf{u} + i\omega\frac{\eta}{\kappa}\mathbf{w} - \nabla P_f = 0,$ (38b)

281     $\boldsymbol{\sigma} = [(H_U - 2\mu)\nabla\cdot\mathbf{u} + \alpha M\nabla\cdot\mathbf{w}]\mathbf{I} + \mu(\nabla\mathbf{u} + \nabla\mathbf{u}^T),$ (38c)

282     $-P_f = \alpha M\nabla\cdot\mathbf{u} + M\nabla\cdot\mathbf{w}.$ (38d)

283   By discretizing Eqs. (38a)-(38d) using second-order differences, we can obtain:

284     $\omega^2\rho u_{x\,i,j} + \omega^2\rho_f w_{x\,i,j} + \frac{\sigma_{xx\,i+1,j}-\sigma_{xx\,i,j}}{\Delta} + \frac{\sigma_{xz\,i,j+1}-\sigma_{xz\,i,j}}{\Delta} = 0,$ (39a)

285     $\omega^2\rho u_{x\,i,j} + \omega^2\rho_f w_{x\,i,j} + \frac{\sigma_{xx\,i+1,j}-\sigma_{xx\,i,j}}{\Delta} + \frac{\sigma_{xz\,i,j+1}-\sigma_{xz\,i,j}}{\Delta} = 0,$ (39b)

286     $\omega^2\rho_f u_{x\,i,j} + i\omega\frac{\eta}{\kappa}w_{x\,i,j} - \frac{P_{f\,i+1,j}-P_{f\,i,j}}{\Delta} = 0,$ (39c)

287     $\omega^2\rho_f u_{z\,i,j} + i\omega\frac{\eta}{\kappa}w_{z\,i,j} - \frac{P_{f\,i,j+1}-P_{f\,i,j}}{\Delta} = 0,$ (39d)

288     $\sigma_{xx\,i,j} = H_U\frac{u_{x\,i+1,j}-u_{x\,i,j}}{\Delta} + (H_U-2\mu)\frac{u_{z\,i,j+1}-u_{z\,i,j}}{\Delta} + \alpha M\left(\frac{w_{x\,i+1,j}-w_{x\,i,j}}{\Delta} + \frac{w_{z\,i,j+1}-w_{z\,i,j}}{\Delta}\right),$ (39e)

289     $\sigma_{zz\,i,j} = (H_U-2\mu)\frac{u_{x\,i+1,j}-u_{x\,i,j}}{\Delta} + H_U\frac{u_{z\,i,j+1}-u_{z\,i,j}}{\Delta} + \alpha M\left(\frac{w_{x\,i+1,j}-w_{x\,i,j}}{\Delta} + \frac{w_{z\,i,j+1}-w_{z\,i,j}}{\Delta}\right),$ (39f)

290     $\sigma_{xz\,i,j} = \mu\left(\frac{u_{x\,i,j+1}-u_{x\,i,j}}{\Delta} + \frac{u_{z\,i+1,j}-u_{z\,i,j}}{\Delta}\right),$ (39g)

291     $-P_f = \alpha M\frac{u_{x\,i+1,j}-u_{x\,i,j}}{\Delta} + \alpha M\frac{u_{z\,i,j+1}-u_{z\,i,j}}{\Delta} + M\left(\frac{w_{x\,i+1,j}-w_{x\,i,j}}{\Delta} + \frac{w_{z\,i,j+1}-w_{z\,i,j}}{\Delta}\right).$ (39h)

292   In the presence of horizontal fracture passing through the numerical cell (i, j_0), the PLSM can be written as:

293    $u_{x\,i,j_0+1} - u_{x\,i,j_0} = (Z_T \sigma_{xz})_{i,j_0},$ (40a)

294    $u_{z\,i,j_0+1} - u_{z\,i,j_0} = \left(Z_{N_D}\sigma_{zz} + Z_{N_D}\alpha P_f\right)_{i,j_0},$ (40b)

295    $w_{z\,i,j_0+1} - w_{z\,i,j_0} = -\left(\alpha Z_{N_D}\sigma_{zz} + \frac{\alpha Z_{N_D}}{B}P_f\right)_{i,j_0}.$ (40c)

296   Rearrange the Eqs. (39e)-(39h), i.e. use the displacement components to represent the stress components, and superimpose the

297   discrete Eqs. (40a)-(40c), we get the following discrete equations:

298    $\frac{u_{x\,i+1,j_0}-u_{x\,i,j_0}}{\Delta} = \left[\frac{H_D}{4\mu(H_D-\mu)}\sigma_{xx} + \frac{(2\mu-H_D)}{4\mu(H_D-\mu)}\sigma_{zz} + \frac{2\alpha\mu}{4\mu(H_D-\mu)}P_f\right]_{i,j_0},$ (41a)

299    $\frac{u_{z\,i,j_0+1}-u_{z\,i,j_0}}{\Delta} = \left[\frac{(2\mu-H_D)}{4\mu(H_D-\mu)}\sigma_{xx} + \left[\frac{H_D}{4\mu(H_D-\mu)}+\frac{Z_{N_D}}{\Delta}\right]\sigma_{zz} + \left[\frac{2\alpha\mu}{4\mu(H_D-\mu)}+\frac{\alpha Z_{N_D}}{\Delta}\right]P_f\right]_{i,j_0},$ (41b)

300    $\frac{u_{x\,i,j_0+1}-u_{x\,i,j_0}}{\Delta} + \frac{u_{z\,i+1,j_0}-u_{z\,i,j_0}}{\Delta} = \left[\left(\frac{1}{\mu}+\frac{Z_T}{\Delta}\right)\sigma_{xz}\right]_{i,j_0},$ (41c)

301    $\frac{w_{x\,i+1,j_0}-w_{x\,i,j_0}}{\Delta} + \frac{w_{z\,i,j_0+1}-w_{z\,i,j_0}}{\Delta} = \left[\frac{2\alpha\mu}{4\mu(H_D-\mu)}\sigma_{xx} + \left(\frac{2\alpha\mu}{4\mu(H_D-\mu)}-\frac{\alpha Z_{N_D}}{\Delta}\right)\sigma_{zz} - \frac{1}{M}\left(\frac{H_U-\mu}{H_D-\mu}+\frac{H_U Z_{N_D}}{\Delta}\right)P_f\right]_{i,j_0}.$ (41d)

302   For a numerical cell, if $j \neq j_0$, we set $Z_{N_D} = Z_T = 0$. By re-injecting Eqs. (41a)-(41d) into the discretized Eqs. (39a)-(39c),

303   we eliminate the stress terms and obtain the compact discretized system of wave equations that contain only the displacement

304   field:

305    $\begin{bmatrix} \mathbf{G}_{11} & \mathbf{G}_{12} & \mathbf{G}_{13} & \mathbf{G}_{14} \\ \mathbf{G}_{21} & \mathbf{G}_{22} & \mathbf{G}_{23} & \mathbf{G}_{24} \\ \mathbf{G}_{31} & \mathbf{G}_{32} & \mathbf{G}_{33} & \mathbf{G}_{34} \\ \mathbf{G}_{41} & \mathbf{G}_{42} & \mathbf{G}_{43} & \mathbf{G}_{44} \end{bmatrix} \begin{bmatrix} \mathbf{u}_x \\ \mathbf{u}_z \\ \mathbf{w}_x \\ \mathbf{w}_z \end{bmatrix} = \begin{bmatrix} \mathbf{0} \\ \mathbf{0} \\ \mathbf{0} \\ \mathbf{0} \end{bmatrix},$ (42)

306   where blocks $\mathbf{G}_{ij}$ $(i, j = 1 \dots 4)$ form the stiffness matrices of the discretized system of the poroelastic wave equations. The

307   poroelastic modeling based on PLSM will be used to validate the other modeling schemes.

308   **6. Numerical examples**

| **Table1** Physical Properties of the Materials Employed in the Numerical Modeling			
Parameters	Background	Fracture	Underlying
Porosity, ϕ	0.15	0.8	0.05
Permeability, κ	0.1 D	100 D	0.01 D
Solid bulk modulus, K_s	36 GPa	36 GPa	36 GPa
Frame bulk modulus, K_m	20.3 GPa	0.055 GPa	30.6 GPa
Frame shear modulus, μ_m	18.6 GPa	0.033 GPa	32.2 GPa
Solid density, ρ_s	2700 kg/m³	2700 kg/m³	2700 kg/m³
Fluid density, ρ_f	1000 kg/m³	1000 kg/m³	1000 kg/m³
Fluid shear viscosity, η_f	0.01 Poise	0.01 Poise	0.01 Poise
Fluid bulk modulus, K_f	2.25 GPa	2.25 GPa	2.25 GPa
Thickness, h		1 mm	

309   In this section, we apply different numerical modeling schemes on three fractured models to examine the FPD effects on

310   seismic wave scattering. We mainly focus on the amplitudes and phases of the scattered and reflected waves generated by

pressure source and shearing source.

6.1 Single horizontal fracture model

Here, we numerically simulate the scattering of seismic waves from a single horizontal fracture embedded in a homogeneous

background. The model measures $2000m \times 1500m$ with a grid interval 5m (namely, the numerical grids size is 401×301)

surrounded by a 200m thick PML boundary. The fracture is located 750m directly below the source $(1000m, 30m)$, with a

500m horizontal extending. A Ricker wavelet with a central frequency of 35Hz is used as the temporal source excitation. The

material properties of the fracture and background are given in Table 1 modified from Nakagawa and Schoenberg (2007) and

Barbosa et al. (2016a). For comparison, we present the seismic wavefields obtained using the poroelastic modeling based on

PLSM, the viscoelastic modeling based on VLSM, as well as the elastic modeling based on LFLSM and HFLSM. To further

study the impact of FPD effects on P- and S-wave, we also apply the pressure source and shearing source in all four schemes,

respectively.
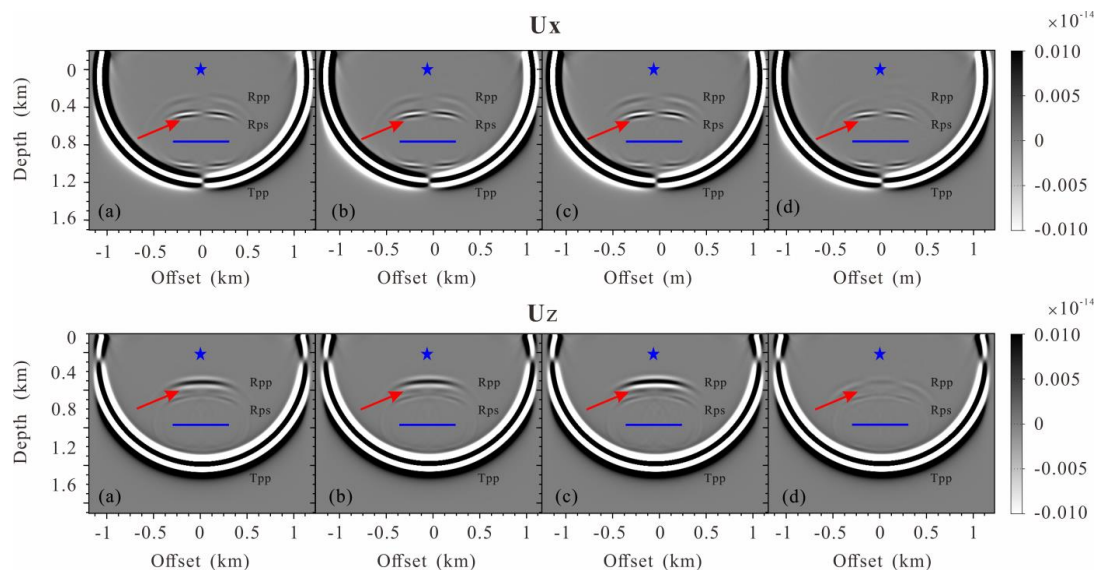
Figure 1: Snapshots of the wavefields components Ux and Uz for a single horizontal fracture model at 280ms due to a P-wave point source: (a) the PLSM based poroelastic modeling, (b) the VLSM based viscoelastic modeling, (c) the LFLSM based elastic modeling and (d) the HFLSM based elastic modeling.

326
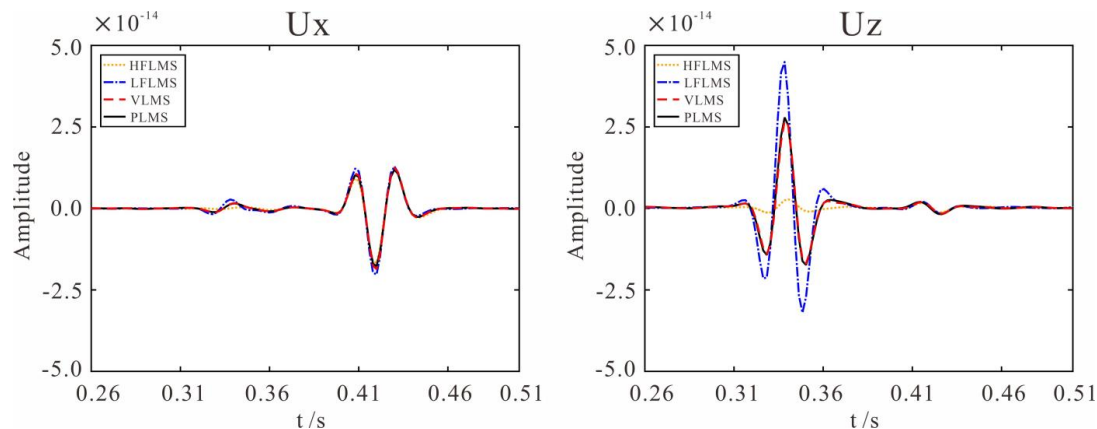
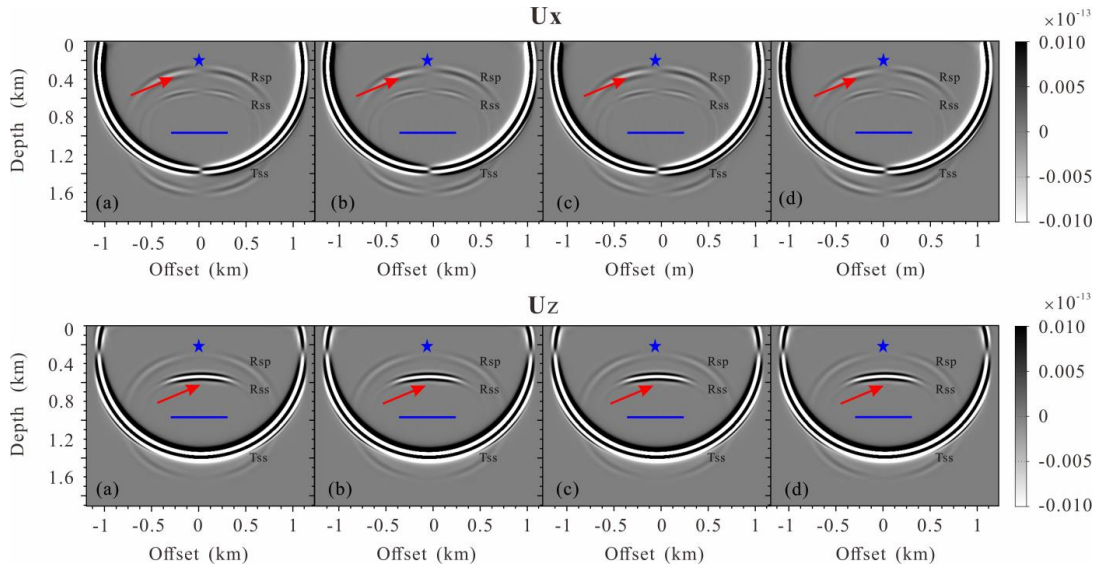**Figure 2: Comparison of 1-D seismograms components Ux and Uz at (1200m, 0m) for a single horizontal fracture model due to a P-wave point source.**
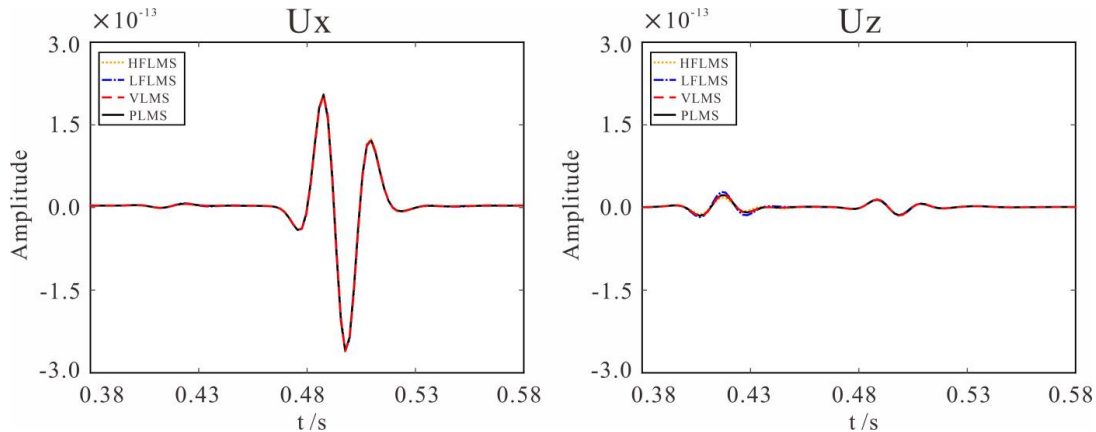
327
328

329   Figure 1 shows the 280ms snapshots of the displacement fields for the single horizontal fracture model models with P-wave

330   point source. The displacement fields are calculated by the PLSM-based poroelastic modeling, the VLSM-based viscoelastic

331   modeling, the LFLSM-based elastic modeling and the HFLSM-based elastic modeling, respectively. The asterisk represents

332   the source and the blue line represents the fracture. To make the small scattered wave visible, large amplitude is clipped, thus

333   the transmitted compressional wave (T_{PP}), scattered compressional wave (S_{PP}) and scattered converted wave (S_{PS}) can be seen

334   clearly. Figure 2 present the comparison of 1-D seismograms at (1200m, 0m).

335   We consider the poroelastic modeling as a reference scenario because it can naturally incorporate the FPD effects. Figure 1

336   and Figure 2 suggest very good agreement between the S_{PP} amplitude calculated using the PLSM-based and VLSM-based

337   modeling, while the HFLSM-based modeling obviously underestimate the S_{PP} amplitude, and the LFLSM-based modeling

338   overestimate the S_{PP} amplitude. This is to be expected, since the scattering behavior of a fracture is mainly controlled by the

339   stiffness contrast with respect to the background. The HFLSM assumes there is insufficient time for fluid exchange at the

340   fracture interface, the fracture behaves as being sealed and the stiffness of the saturated fracture is maximal, resulting in an

341   underestimated stiffness contrast between fracture and background. The LFLSM assumes there is enough time for fluid flow

342   between the fracture and background, the deformation of the fracture is maximal, resulting in an overestimated stiffness

343   contrast with background. However, the VLSM derived from poroelastic theory can properly incorporate the FPD effects,

344   leading to a frequency-dependent stiffness contrast equivalent to the PLSM. It can be note that the S_{PP} amplitudes obtained

345   using the LFLSM-based modeling is comparable to that of the PLSM based modeling, because the FPD effects mainly occur

346   at seismic frequencies closer to the low frequency limit. The S_{PP} travel time obtained using the four modeling schemes shows

347   good consistency. Figure 2 also shows that the discrepancy of the S_{PS} amplitudes is almost negligible. Figure 1 and Figure 2

348   demonstrate that the DLSM-based viscoelastic modeling can appropriately capture the FPD effects on wave scattering of a

349   fluid saturated fracture. However, the two elastic modeling cannot correctly estimate the S_{PP} amplitudes.

Figure 3: Snapshots of the wavefields components Ux and Uz for a single horizontal fracture model at 280ms due to a S-wave point source: (a) the PLSM based poroelastic modeling, (b) the VLSM based viscoelastic modeling, (c) the LFLSM based elastic modeling and (d) the HFLSM based elastic modeling.

Figure 4: Comparison of 1-D seismograms components Ux and Uz at receiver (1200m, 0m) for a single horizontal fracture model due to a S-wave point source.

Figure 3 shows the 360ms snapshots of the displacement fields for the single horizontal fracture model models with S-wave point source. Figure 4 is the comparison of 1-D seismograms at (1200m,0m). Figure 3 and Figure 4 show that the amplitudes of the calculated S_{SP} and S_{SS} using four modeling schemes have good consistency, indicating that S-wave point source exploration survey is less sensitive to fluids or FDP effects for a single fracture. The scattering behavior is mainly controlled by the drained stiffness contrast between the fracture and the background.

6.2 Fractured reservoir model

In addition to a single fracture, we are more interested in the scattering behavior of discretely distributed fractures system. To

14

364   this end, we designed a fractured reservoir model containing a conjugate fracture system (consisting of two sets of mutually

365   perpendicular fractures, as illustrated in Figure 5). The normal spacing and extending of this set of conjugate fractures are

366   1.768m and 70.7m, respectively. The material properties of the fracture, background (yellow region) and underlying (green

367   region) formation are given in Table 1. The model size, grid interval and source location are the same as those in the previous

368   numerical examples.
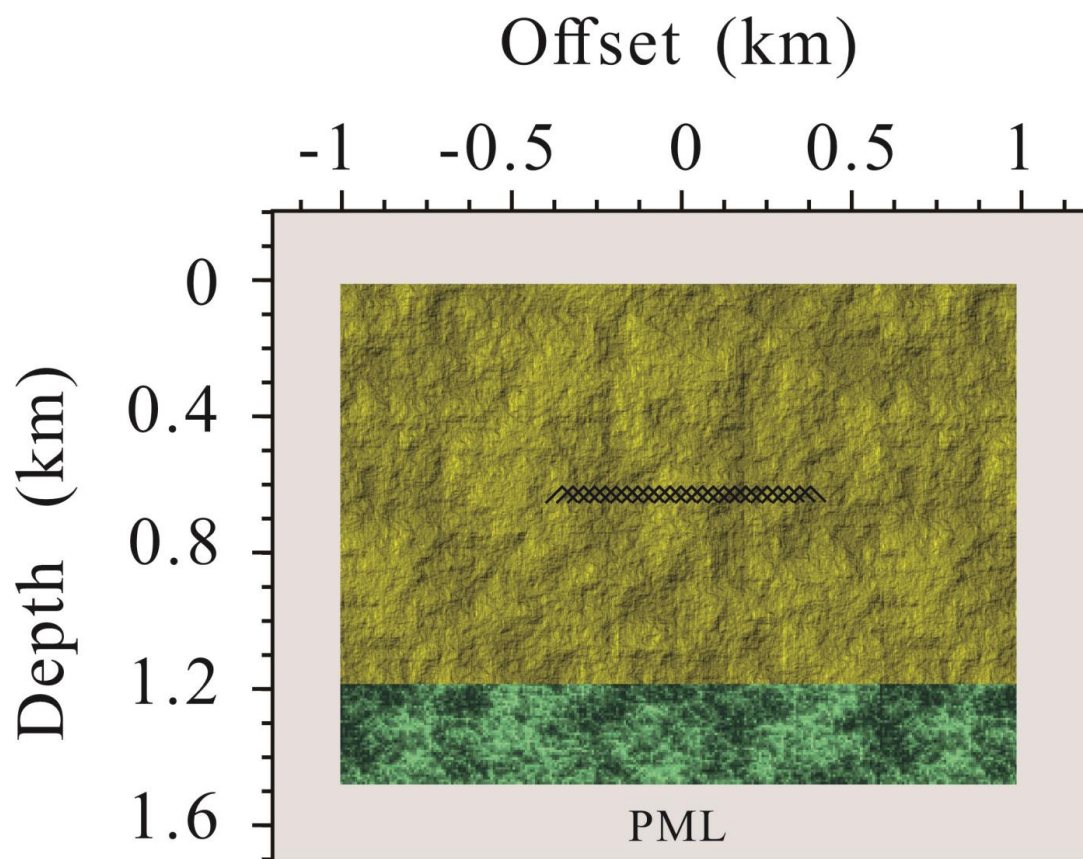
369

370   **Figure 5: Schematic diagram of the fractured reservoir model I with a conjugate fracture system. The black segments present the**

371   **fracture system. The normal spacing and extending of each fracture are 1.768m and 70.7m, respectively.**
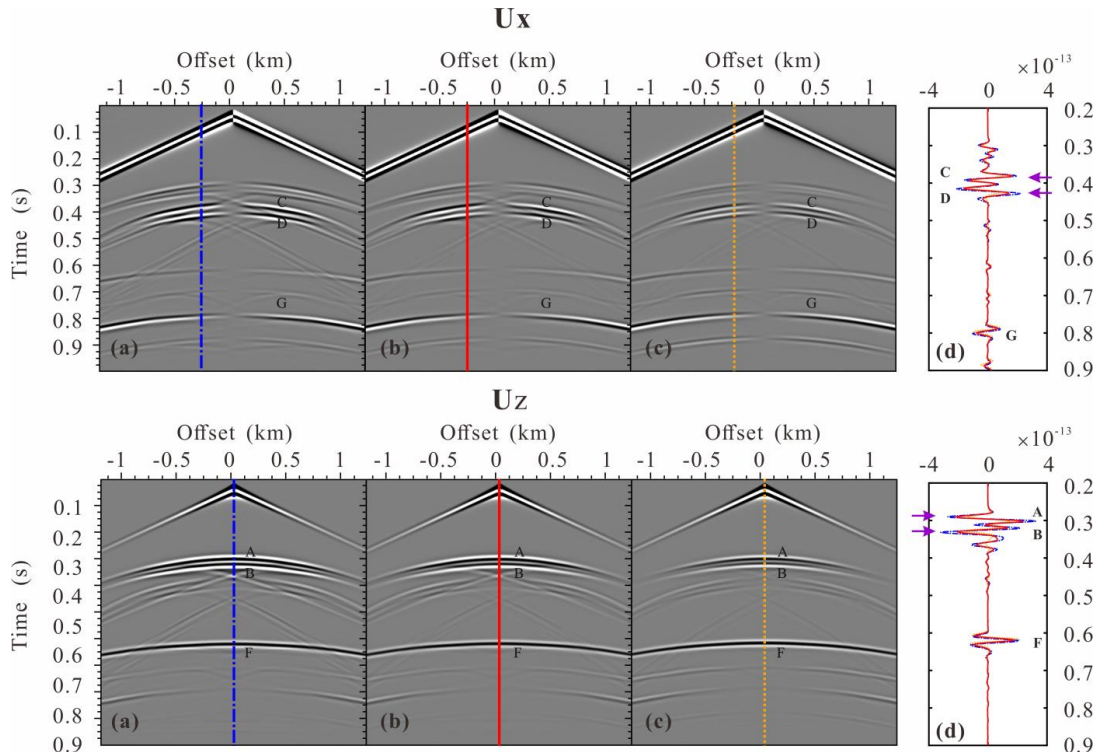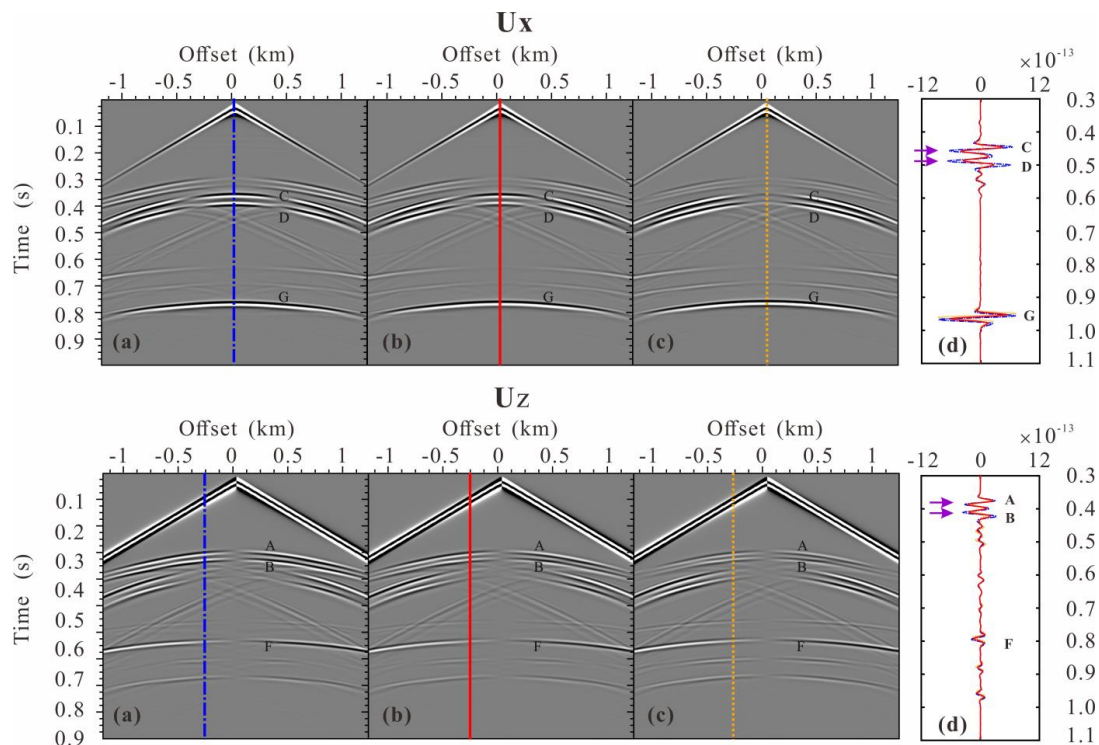
Figure 6: Seismogram components Ux and Uz of the fractured reservoir model I due to a P-wave point source: calculated using (a) the LFLSM, (b) the VLSM, (c) the HFLSM. (d) is the comparison of single trace extracted from the three gathers. A and B are scattered compressional wave from top and bottom, respectively, C and D are scattered converted wave top and bottom, respectively, F and G are reflected compressional wave and converted wave, respectively, E is scattered diffracted wave.

Figure 6 presents the seismograms of fractured reservoir model I for a P-wave point source. The scattered compressional wave (S_{PP}) and scattered converted wave (S_{PS}) from the top and bottom of the fractured reservoir, the reflected compressional wave (R_{PP}), converted wave (R_{PS}) from the underlying formation, diffracted wave at the edge of the fractured reservoir can be clearly identified. Similar to the single fracture case, the amplitude of the S_{PP} from the top of the fractured reservoir obtained by the HFLSM-based modeling is weakest (underestimated), that obtained by LFLSM-based modeling is strongest (overestimated), and that obtained by the VLSM-based modeling is intermediate (accurate). The purple arrows in the Figure 6 (d) indicate that the S_{PP} from the bottom of the fractured reservoir obtained by the LFLSM-based and HFLSM-based modeling has a slightly larger amplitude than that from the top, while the S_{PP} from the bottom of the fractured reservoir obtained by the VLSM-based modeling has a slightly smaller amplitude than that from the top. This is expected, since the VLSM-based modeling scheme can capture the wave attenuation and dispersion due to the FDP effects between the fracture system and background, while the LFLSM and HFLSM represent non-attenuated and non-dispersive elastic processes. However, due to the weak degree of dispersion, the S_{PP} travel time obtained by the three modeling schemes is almost consistent. Figure 6 shows that the amplitudes of the R_{PP} from the underlying formation calculated by the HFLSM-based and LFLSM-based modeling are almost equal, while

16

390 that calculated by the VLSM-based modeling is attenuated and dispersed. That again indicates the VLSM-based modeling can

391 capture the FPD effects. The S_{PS} and R_{PS} show similar behavior as the S_{PP} and R_{PP}. Figure 6 suggests that the scattered waves

392 from the bottom of the fractured reservoir are attenuated and dispersed by the FPD effects and the reflected waves can retain

393 the relevant attenuation and dispersion information.

394
395 **Figure 7: Seismogram components Ux and Uz of the fractured reservoir model I due to a S-wave point source: calculated using (a)**
396 **the LFLSM, (b) the VLSM, (c) the HFLSM. (d) is the comparison of single trace extracted from the three gathers. A, B are scattered**
397 **converted SP-wave from top and bottom, respectively, C and D are scattered shear SS-wave from top and bottom, respectively, F**
398 **and G are reflected converted SP-wave and shear SS-wave, respectively, E is scattered diffracted wave.**

399 Figure 7 presents the seismograms of fractured reservoir model I for a S-wave point source. The scattered converted wave (S_{SP})

400 and shearing wave (S_{SS}) from the top and bottom of the fractured reservoir, the reflected converted wave (R_{SP}) and shearing

401 wave (R_{SS}) from the underlying formation can be identified in Figure 7. Unlike the case of single horizontal fracture, the FPD

402 effects between a conjugate fracture system and background can attenuate and disperse the S_{PP}, S_{PS}, R_{PP} and R_{PS} for a S-wave

403 point source exploration survey.
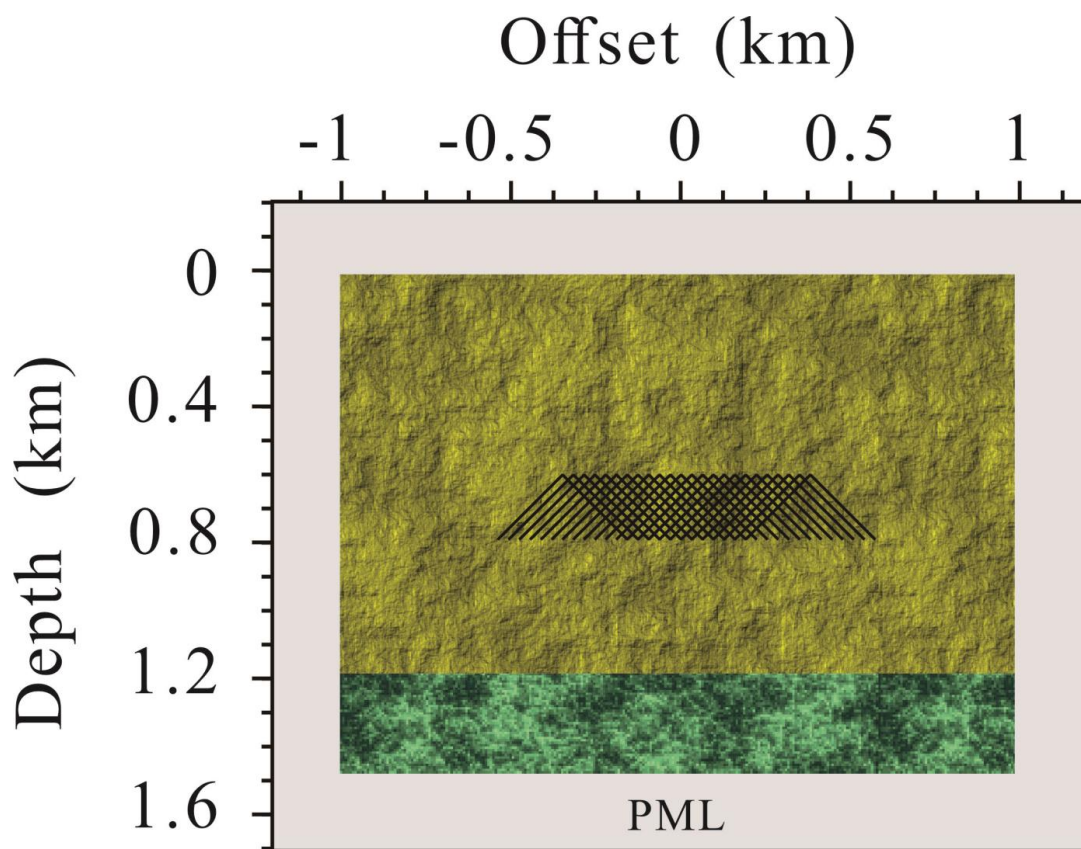
Figure 8: Schematic diagram of the fractured reservoir model II. The normal spacing and extending of each fracture are 1.768m and 282.8m, respectively.

The attenuation and dispersion caused by FDP effects are strongly affected by the thickness of the reservoir. In general, the thicker the fractured reservoir, the more severe attenuation and dispersion of the seismic wave. To demonstrate the strong attenuation and dispersion caused by FDP effect, we modify the fractured model I, increase each fracture to 282.8m without changing other parameters, and obtain a fractured model II. Figure 9 presents the seismograms of fractured reservoir model II for a P-wave point source. Figure 9 shows that the S_{PP} and S_{PS} from the bottom of the fractured reservoir and the R_{PP} and R_{PS} from the underlying formation obtained by the VLSM-based modeling are strongly attenuated and dispersed, proving that the VLSM-based modeling can be captured the FPD effects when seismic waves travel through the fractured reservoir. Figure10 presents the seismograms of the fractured reservoir model II for a S-wave point source. Figure 10 shows that the scattered and reflected waves obtained by VLSM-based modeling are also strongly attenuated and dispersed.
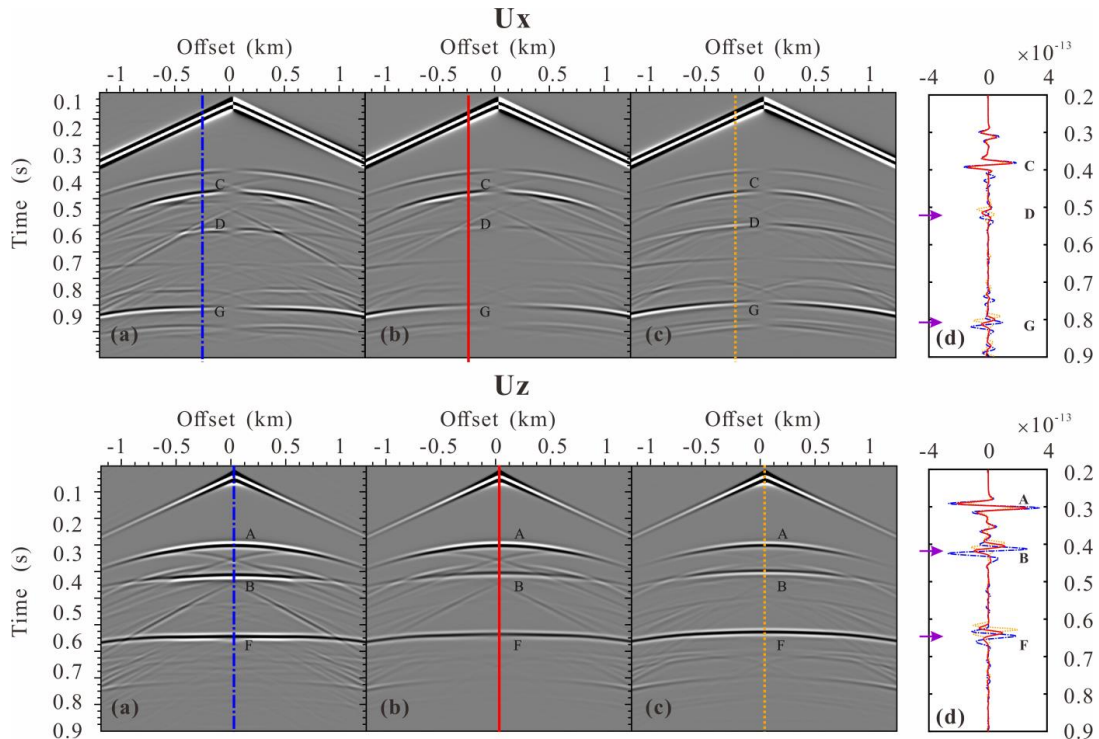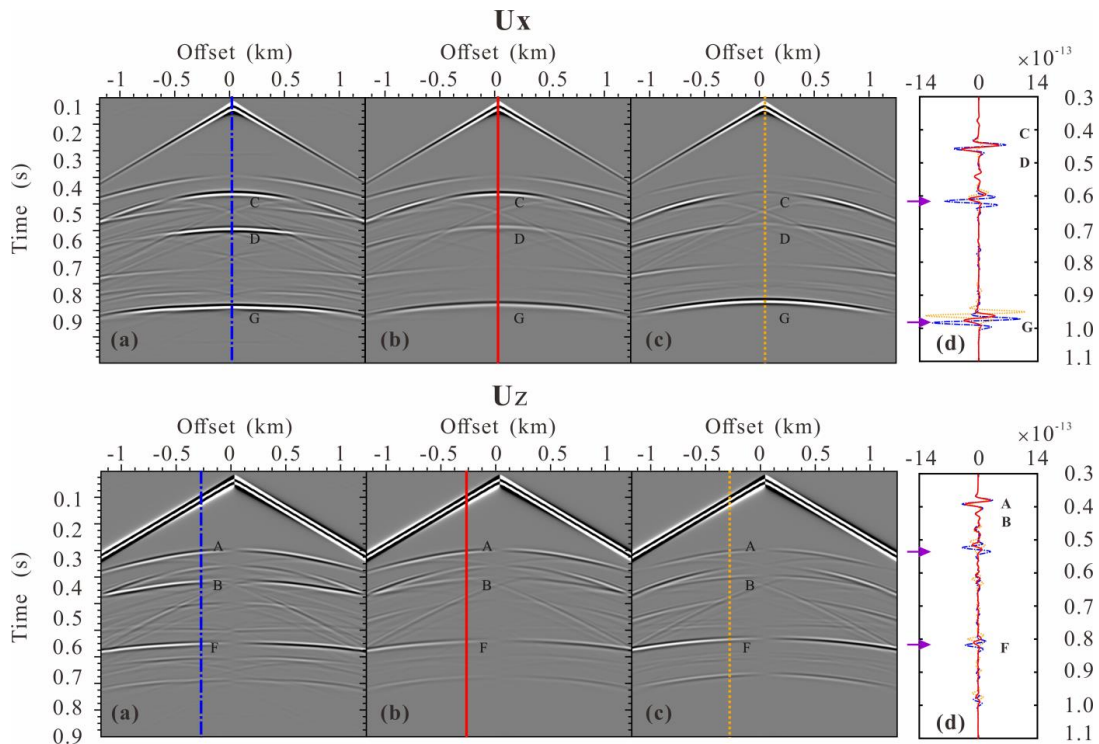
Figure 9: Seismogram components Ux and Uz of the fractured reservoir model II due to a P-wave point source: calculated using (a) the LFLSM, (b) the VLSM, (c) the HFLSM. (d) is the comparison of single trace extracted from the three gathers. The meanings of A, B, C, D, E, F and G are same as those in Figure 9.
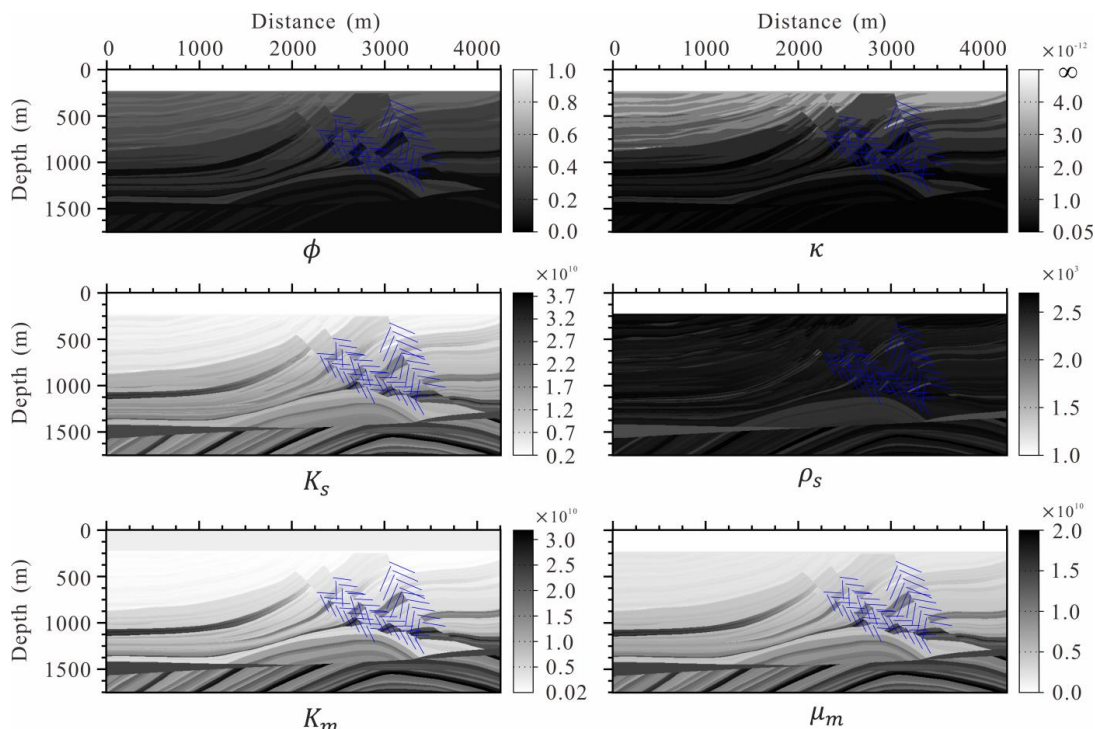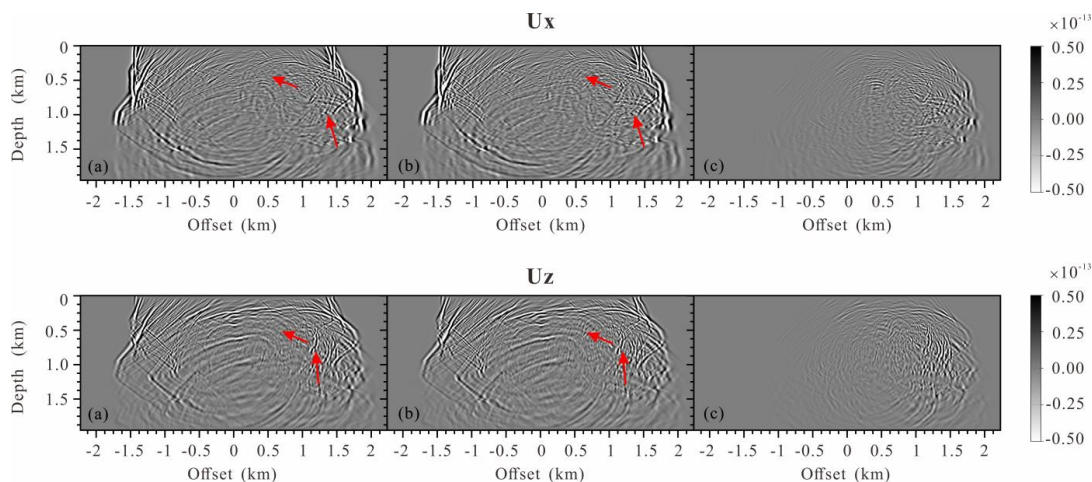
421   **Figure 10: Seismogram components Ux and Uz of the fractured reservoir model I due to a S-wave point source: calculated using (a)**

422   **the LFLSM, (b) the VLSM, (c) the HFLSM. (d) is the comparison of single trace extracted from the three gathers. The meanings of**

423   **A, B, C, D, E, F and G are same as those in Figure 10.**

424   **6.3 Modified Marmousi model**

425

426   **Figure 11: The physical properties and elastic modulus models of the modified Marmousi model.**

427   We test the proposed VLSM-based modeling scheme on a more complex modified Marmousi model. To modify the Marmousi

428   model, we generate a porosity model, permeability model and discrete large-scale fracture system, and transform the original

429   P-wave velocity and density into the fluid saturated bulk and shear modulus of the background by a constant Poisson's ratio

430   0.5, and finally obtain the grain bulk modulus, the frame bulk and shear modulus of the background through Gassmann

431   equation and empirical formula ($K_m = (1 - \phi)^{3/(1-\phi)} K_s$). The input physical properties and elastic modulus models of the

432   modified Marmousi model are present in Figure 11. The fluid density, bulk modulus and viscosity are the same as in Table 1.

433   The model size is 4250m×1750m with grid interval 5m and a 100m thick PML boundary. The source is located at the surface

434   (2125m, 0m). A Ricker wavelet with a central frequency of 25Hz is used as the temporal source excitation.

Figure 12: Snapshots of the wavefields components Ux and Uz at 1000ms: (a) the original Marmousi model without fractures, (b) the modified Marmousi model with fractures and (c) the differences.
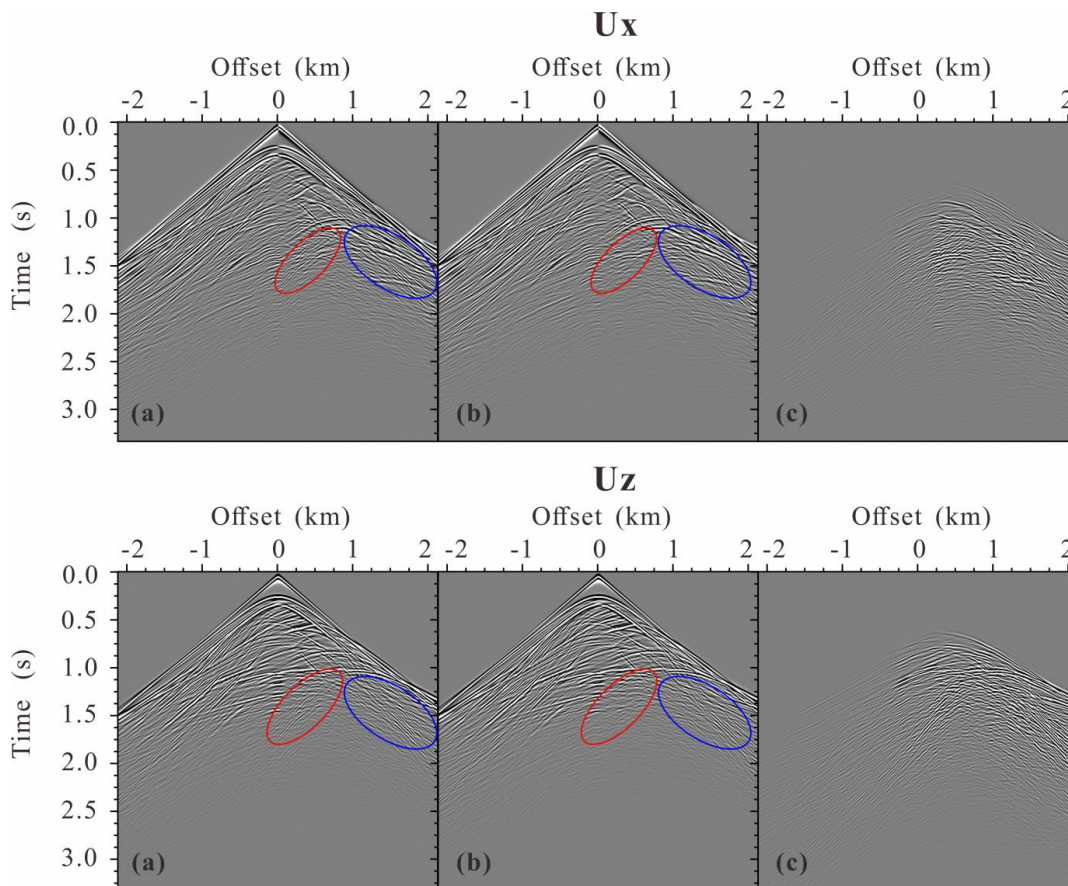
Figure 13: Seismogram components Ux and Uz: (a) the modified Marmousi model with fractures, (b) the original Marmousi model without fractures and (c) the differences.

Figures 12 shows the snapshots of displacement fields at 1000ms. The figure clearly shows the scattered P- and S-waves by

442   the discrete distributed large-scale fractures. The results with such a complex model clearly verify the numerical

443   implementation and the code. We also calculate the seismograms of the displacement shown in Figure 13. The seismograms

444   obtained by our proposed modeling scheme present the scattered seismic waves by the discrete fractures.

445   **7. Conclusions**

446   In this work, we have developed a numerical modeling scheme including FPD effects for discrete distributed large-scale

447   fractures embedded in fluid saturated porous rock. To capture the FPD effects between the fractures and background, the

448   fractures are represented as Barbosa's VLSM with complex-valued and frequency-dependent fracture compliances. Using

449   Coates and Schoenberg's local effective medium theory and Barbosa's VLSM, we derive the effective anisotropic viscoelastic

450   compliances in each spatial discretized cell by superimposing the compliances of the background and the fractures. The local

451   effective governing equations of numerical cells are expressed by the derived effective compliances and discretized by mixed-

452   grid stencil FDFD. The proposed modeling scheme can be used to study the impact of mechanical and hydraulic of fracture

453   properties on seismic scattering.

454   The numerical results of the single horizontal fracture model with a P-point source valid that the proposed VLSM-based

455   modeling can include the FPD effects and thus accurately estimate the scattered wave of the horizontal fracture. In contrast,

456   the LFLSM-based modeling overestimates the scattered wave and the HFLSM-based modeling underestimates the scattered

457   wave. The numerical results with an S-point source show that the scattered waves off a single horizontal fracture is less

458   sensitive to FDP effects. Due to the differences in fracture orientation, the results of the conjugate fractured reservoir model

459   are quite different from those of the single horizontal fracture model. For both P- and S-point sources, the amplitudes of the

460   scattered waves from the top of the fractured reservoir are affected by the fluid stiffening effects due to the FPD effects. The

461   scattered waves from the bottom of the fractured reservoir are also attenuated and dispersed by the FPD effects in addition to

462   the fluid stiffening effects and the reflected waves can retain the relevant attenuation and dispersion information. The results

463   of the modified Marmousi model clearly show the scattered P- and S-waves by the discrete distributed large-scale fractures

464   and verify the proposed numerical modeling scheme. The proposed numerical modeling scheme is expected not only to

465   improve the estimations of seismic wave scattering from discrete distributed large-scale fractures but can also to improve

466   migration quality and the estimation of fracture mechanical characteristics in inversion.

467   **Appendix A: The coefficients related to spatial derivative operators**

468   We define coefficient vectors $\mathbf{T}_k (k = 1,2,3,4)$ and the derivative operate vector $\mathbf{D}(c)$ as

469    $\mathbf{T}_1 = \frac{1}{\xi_x \xi_x}[1 \quad 0 \quad 0 \quad 0]$, $\mathbf{T}_2 = \frac{1}{\xi_x \xi_z}[0 \quad 1 \quad 0 \quad 0]$, $\mathbf{T}_3 = \frac{1}{\xi_x \xi_z}[0 \quad 0 \quad 1 \quad 0]$, $\mathbf{T}_4 = \frac{1}{\xi_z \xi_z}[0 \quad 0 \quad 0 \quad 1]$,   (A-1)

470    $\mathbf{D}(c) = [\partial_x(c\partial_x) \quad \partial_x(c\partial_z) \quad \partial_z(c\partial_x) \quad \partial_z(c\partial_z)]$,   (A-2)

471   where ξ_x and ξ_z are the PML damping function, c represents effective stiffness. Then, the expression of A_c, B_c, C_c, D_c are

472   written in matrix form:

473
$$\begin{bmatrix} A_c \\ B_c \\ C_c \\ D_c \end{bmatrix} = \begin{bmatrix} \mathbf{D}(c_{11}) & \mathbf{D}(c_{15}) & \mathbf{D}(c_{15}) & \mathbf{D}(c_{55}) \\ \mathbf{D}(c_{15}) & \mathbf{D}(c_{55}) & \mathbf{D}(c_{13}) & \mathbf{D}(c_{35}) \\ \mathbf{D}(c_{15}) & \mathbf{D}(c_{13}) & \mathbf{D}(c_{55}) & \mathbf{D}(c_{35}) \\ \mathbf{D}(c_{55}) & \mathbf{D}(c_{35}) & \mathbf{D}(c_{35}) & \mathbf{D}(c_{33}) \end{bmatrix} \begin{bmatrix} \mathbf{T}_1 \\ \mathbf{T}_2 \\ \mathbf{T}_3 \\ \mathbf{T}_4 \end{bmatrix}.$$
(A-3)

474   We formulate A_r, B_r, C_r, D_r in a similar way by defining the coefficient vectors $\mathbf{T}'_k (k = 1,2,3,4)$ and $\mathbf{D}'(c)$ as

475    $\mathbf{T}'_1 = \frac{1}{2\xi_x\xi_x}[1 \quad 1 \quad 1 \quad 1]^T$, $\mathbf{T}'_2 = \frac{1}{2\xi_x\xi_z}[-1 \quad 1 \quad -1 \quad 1]^T$,

476    $\mathbf{T}'_3 = \frac{1}{2\xi_x\xi_z}[-1 \quad -1 \quad 1 \quad 1]^T$, $\mathbf{T}'_4 = \frac{1}{2\xi_z\xi_z}[1 \quad -1 \quad -1 \quad 1]^T$,
(A-4)

477    $\mathbf{D}'(c) = [\partial_{x'}(c\partial_{x'}) \quad \partial_{x'}(c\partial_{z'}) \quad \partial_{z'}(c\partial_{x'}) \quad \partial_{z'}(c\partial_{z'})]$.
(A-5)

478   The expression of A_r, B_r, C_r, D_r are written as

479
$$\begin{bmatrix} A_r \\ B_r \\ C_r \\ D_r \end{bmatrix} = \begin{bmatrix} \mathbf{D}'(c_{11}) & \mathbf{D}'(c_{15}) & \mathbf{D}'(c_{15}) & \mathbf{D}'(c_{55}) \\ \mathbf{D}'(c_{15}) & \mathbf{D}'(c_{55}) & \mathbf{D}'(c_{13}) & \mathbf{D}'(c_{35}) \\ \mathbf{D}'(c_{15}) & \mathbf{D}'(c_{13}) & \mathbf{D}'(c_{55}) & \mathbf{D}'(c_{35}) \\ \mathbf{D}'(c_{55}) & \mathbf{D}'(c_{35}) & \mathbf{D}'(c_{35}) & \mathbf{D}'(c_{33}) \end{bmatrix} \begin{bmatrix} \mathbf{T}'_1 \\ \mathbf{T}'_2 \\ \mathbf{T}'_3 \\ \mathbf{T}'_4 \end{bmatrix}.$$
(A-6)

480   **Appendix B: Parsimonious staggered-grid stencil**

481   The nine coefficients of the CS stencil for the submatrix $\mathbf{A}_c$ of Eq. (36):

482    $A_{c\,i+1,j} = \frac{c_{11\,i+\frac{1}{2},j}}{\Delta^2\xi_{x\,i}\xi_{x\,i+\frac{1}{2}}}$, $A_{c\,i-1,j} = \frac{c_{11\,i-\frac{1}{2},j}}{\Delta^2\xi_{x\,i}\xi_{x\,i-\frac{1}{2}}}$, $A_{c\,i,j+1} = \frac{c_{55\,i,j+\frac{1}{2}}}{\Delta^2\xi_{z\,j}\xi_{z\,j+\frac{1}{2}}}$, $A_{c\,i,j-1} = \frac{c_{55\,i,j-\frac{1}{2}}}{\Delta^2\xi_{z\,j}\xi_{z\,j-\frac{1}{2}}}$,

483    $A_{c\,i,j} = -\frac{c_{11\,i+\frac{1}{2},j}}{\Delta^2\xi_{x\,i}\xi_{x\,i+\frac{1}{2}}} - \frac{c_{11\,i-\frac{1}{2},j}}{\Delta^2\xi_{x\,i}\xi_{x\,i-\frac{1}{2}}} - \frac{c_{55\,i,j+\frac{1}{2}}}{\Delta^2\xi_{z\,i}\xi_{z\,j+\frac{1}{2}}} - \frac{c_{55\,i,j-\frac{1}{2}}}{\Delta^2\xi_{z\,i}\xi_{z\,j-\frac{1}{2}}}$, $A_{c\,i+1,j+1} = \frac{c_{15\,i+1,j}+c_{15\,i,j+1}}{4\Delta^2\xi_{x\,i}\xi_{z\,j}}$,

484    $A_{c\,i+1,j-1} = -\frac{c_{15\,i+1,j}+c_{15\,i,j-1}}{4\Delta^2\xi_{x\,i}\xi_{z\,j}}$, $A_{c\,i-1,j+1} = -\frac{c_{15\,i-1,j}+c_{15\,i,j+1}}{4\Delta^2\xi_{x\,i}\xi_{z\,j}}$, $A_{c\,i-1,j-1} = \frac{c_{15\,i-1,j}+c_{15\,i,j-1}}{4\Delta^2\xi_{x\,i}\xi_{z\,j}}$.
(B-1)

485   The nine coefficients of the RS stencil for the submatrix $\mathbf{A}_r$ of Eq. (36):

486    $A_{r\,i+1,j} = \frac{c_{11\,i+\frac{1}{2},j-\frac{1}{2}}-c_{55\,i+\frac{1}{2},j-\frac{1}{2}}}{4\Delta^2\xi_{x\,i}\xi_{z\,j-\frac{1}{2}}} + \frac{c_{11\,i+\frac{1}{2},j+\frac{1}{2}}-c_{55\,i+\frac{1}{2},j+\frac{1}{2}}}{4\Delta^2\xi_{z\,j}\xi_{x\,i+\frac{1}{2}}}$, $A_{r\,i-1,j} = \frac{c_{11\,i-\frac{1}{2},j+\frac{1}{2}}-c_{55\,i-\frac{1}{2},j+\frac{1}{2}}}{4\Delta^2\xi_{x\,i}\xi_{z\,j+\frac{1}{2}}} + \frac{c_{11\,i-\frac{1}{2},j-\frac{1}{2}}-c_{55\,i-\frac{1}{2},j-\frac{1}{2}}}{4\Delta^2\xi_{z\,j}\xi_{x\,i-\frac{1}{2}}}$,

487    $A_{r\,i,j+1} = \frac{c_{55\,i-\frac{1}{2},j+\frac{1}{2}}-c_{11\,i-\frac{1}{2},j+\frac{1}{2}}}{4\Delta^2\xi_{x\,i}\xi_{z\,j+\frac{1}{2}}} + \frac{c_{55\,i+\frac{1}{2},j+\frac{1}{2}}-c_{11\,i+\frac{1}{2},j+\frac{1}{2}}}{4\Delta^2\xi_{z\,j}\xi_{x\,i+\frac{1}{2}}}$, $A_{r\,i,j-1} = \frac{c_{55\,i+\frac{1}{2},j-\frac{1}{2}}-c_{11\,i+\frac{1}{2},j-\frac{1}{2}}}{4\Delta^2\xi_{x\,i}\xi_{z\,j-\frac{1}{2}}} + \frac{c_{55\,i-\frac{1}{2},j-\frac{1}{2}}-c_{11\,i-\frac{1}{2},j-\frac{1}{2}}}{4\Delta^2\xi_{z\,j}\xi_{x\,i-\frac{1}{2}}}$,

488    $A_{r\,i,j} = -\frac{c_{11\,i+\frac{1}{2},j-\frac{1}{2}}-2c_{15\,i+\frac{1}{2},j-\frac{1}{2}}+c_{55\,i+\frac{1}{2},j-\frac{1}{2}}}{4\Delta^2\xi_{x\,i}\xi_{x\,i+\frac{1}{2}}} - \frac{c_{11\,i-\frac{1}{2},j+\frac{1}{2}}-2c_{15\,i-\frac{1}{2},j+\frac{1}{2}}+c_{55\,i-\frac{1}{2},j+\frac{1}{2}}}{4\Delta^2\xi_{x\,i}\xi_{x\,i-\frac{1}{2}}} - \frac{c_{11\,i+\frac{1}{2},j+\frac{1}{2}}+2c_{15\,i+\frac{1}{2},j+\frac{1}{2}}+c_{55\,i+\frac{1}{2},j+\frac{1}{2}}}{4\Delta^2\xi_{z\,j}\xi_{z\,j+\frac{1}{2}}} - \frac{c_{11\,i-\frac{1}{2},j-\frac{1}{2}}+2c_{15\,i-\frac{1}{2},j-\frac{1}{2}}+c_{55\,i-\frac{1}{2},j-\frac{1}{2}}}{4\Delta^2\xi_{z\,j}\xi_{z\,j-\frac{1}{2}}}$,

489    $A_{r\,i+1,j+1} = \frac{c_{11\,i+\frac{1}{2},j+\frac{1}{2}}+2c_{15\,i+\frac{1}{2},j+\frac{1}{2}}+c_{55\,i+\frac{1}{2},j+\frac{1}{2}}}{4\Delta^2\xi_{z\,j}\xi_{z\,j+\frac{1}{2}}}$, $A_{r\,i+1,j-1} = \frac{c_{11\,i+\frac{1}{2},j-\frac{1}{2}}-2c_{15\,i+\frac{1}{2},j-\frac{1}{2}}+c_{55\,i+\frac{1}{2},j-\frac{1}{2}}}{4\Delta^2\xi_{x\,i}\xi_{x\,i+\frac{1}{2}}}$,

490    $A_{r\,i-1,j+1} = \frac{c_{11\,i-\frac{1}{2},j+\frac{1}{2}}-2c_{15\,i-\frac{1}{2},j+\frac{1}{2}}+c_{55\,i-\frac{1}{2},j+\frac{1}{2}}}{4\Delta^2\xi_{x\,i}\xi_{x\,i-\frac{1}{2}}}$, $A_{r\,i-1,j-1} = \frac{c_{11\,i-\frac{1}{2},j-\frac{1}{2}}+2c_{15\,i-\frac{1}{2},j-\frac{1}{2}}+c_{55\,i-\frac{1}{2},j-\frac{1}{2}}}{4\Delta^2\xi_{z\,j}\xi_{z\,j-\frac{1}{2}}}$.
(B-2)

491   The coefficients of the submatrices $\mathbf{B}_c$, $\mathbf{C}_c$, $\mathbf{D}_c$ and $\mathbf{B}_r$, $\mathbf{C}_r$, $\mathbf{D}_r$ can be inferred easily from those of submatrix $\mathbf{A}_c$ and

492    $\mathbf{A}_r$, respectively.

References

Barbosa, N. D., Rubino J. G., Caspari E., and Holliger K.: Extension of the classical linear slipmodel for fluid-saturated fractures: Accounting for fluid pressure diffusion effects, J. Geophys. Res., 122, 1302-1323, doi:10.1002/2016JB013636, 2016a.

Barbosa, N. D., Rubino J. G., Caspari E., Milani M., and Holliger K.: Fluid pressure diffusion effects on the seismic reflectivity of a single fracture, J. Acoust. Soc. Am., 140, 2554-2570, doi:10.1121/1.4964339, 2016b.

Biot, M. A.: Theory of elastic waves in a fluid-saturated porous solid. I. Low frequency range, J. Acoust. Soc. Am., 28, 168-178, doi:10.1121/1.1908239, 1956a.

Biot, M. A.: Theory of elastic waves in a fluid-saturated porous solid. II. High frequency range, J. Acoust. Soc. Am., 28, 179-191, doi:10.1121/1.1908241, 1956b.

Brajanovski, M., Gurevich, B., and Schoenberg, M.: A model for P-wave attenuation and dispersion in a porous medium permeated by aligned fractures, Geophys. J. Int., 163, 372-384, doi:10.1111/j.1365-246X.2005.02722.x, 2005.

Brajanovski, M., Müller T. M., and Gurevich B.: Characteristic frequencies of seismic attenuation due to wave-induced fluid flow in fractured porous media, Geophys. J. Int., 166, 574-578, doi:10.1111/j.1365-246X.2006.03068.x, 2006.

Chapman, M.: Frequency dependent anisotropy due to mesoscale fractures in the presence of equant porosity, Geophys. Prospect., 51, 369-379, doi:10.1046/j.1365-2478.2003.00384.x, 2003.

Coates, R. T. and Schoenberg, M.: Finite-difference modeling of faults and fractures, Geophysics, 60, 1514-1526, doi:10.1190/1.1443884, 1995.

Cui, X. Q., Lines, L. R., and Krebes, E. S.: Seismic modelling for geological fractures, Geophys. Prospect., 2018,157-168, doi:10.1111/1365-2478.12536, 2018.

Dutta, N. C. and Odé, H.: Attenuation and dispersion of compressional waves in fluid-filled porous rocks with partial gas saturation (White Model)-Part I: Biot theory, Geophysics, 44, 1777-1788, doi:10.1190/1.1440938, 1979a.

Dutta, N. C. and Odé, H.: Attenuation and dispersion of compressional waves in fluid-filled porous rocks with partial gas saturation (White Model)-Part II: Results, Geophysics, 44, 1806-1812, doi:10.1190/1.1440939, 1979b.

Gale, J. F. W., Laubach S. E., Olson J. E., Eichhubl P., and Fall A.: Natural fractures in shale: A review and new observations: AAPG Bulletin, 98, 2165-2216, doi:10.1306/08121413151, 2014.

Galvin, R. J. and Gurevich, B.: Frequency-dependent anisotropy of porous rocks with aligned fractures, Geophys. Prospect.,

523   63, 141-150, doi:10.1071/ASEG2003ab016, 2015.

524   Gassmann, F.: Elastic waves through a packing of spheres, Geophysics, 16, 673-685, doi:10.1190/1.1437718, 1951.

525   Gavagnin, C., Sanavia, L., and Lorenzis, L. D.: Stabilized mixed formulation for phase-field computation of deviatoric fracture

526   in elastic and poroelastic materials, Comput Mech, 65, 1447-1465, doi:10.1007/s00466-020-01829-x, 2020.

527   Gelinsky, S. and Shapiro, S. A.: Dynamic-equivalent medium approach for thinly layered saturated sediments, Geophys. J. Int.,

528   128, F1-F4, doi:10.1111/j.1365-246X.1997.tb04086.x, 1997.

529   Guo J. X., Rubino J. G., Barbosa, N. D., Glubokovskikh, S. G., and Gurevich, B.: Seismic dispersion and attenuation in

530   saturated porous rocks with aligned fractures of finite thickness: Theory and numerical simulations—Part I: P-wave

531   perpendicular to the fracture plane, Geophysics, 83, 49-62, doi:10.1190/geo2017-0065.1, 2017a.

532   Guo J. X., Rubino J. G., Barbosa, N. D., Glubokovskikh, S. G., and Gurevich, B.: Seismic dispersion and attenuation in

533   saturated porous rocks with aligned fractures of finite thickness: Theory and numerical simulations—Part II: Frequency-

534   dependent anisotropy, Geophysics, 83, 63-71, doi:10.1190/geo2017-0066.1, 2017b.

535   Gurevich, B., Zyrianov, V. B., and Lopatnikov, S. L.: Seismic attenuation in finely layered porous rocks: Effects of fluid flow

536   and scattering, Geophysics, 62(1), 319-324, doi:10.1190/1.1444133, 1997.

537   Gurevich, B.: Elastic properties of saturated porous rocks with aligned fractures, J. Geophys. Res., 54, 203-218,

538   doi:10.1016/j.jappgeo.2002.11.002, 2003.

539   Hustedt, B., Operto S., and Virieux J.: Mixed-grid and staggered-grid finite difference methods for frequency domain acoustic

540   wave modelling, Geophys J Int, 157, 1269-1296, doi:10.1111/j.1365-246X.2004.02289.x, 2004.

541   Johnson, D. L.: Theory of frequency dependent acoustics in patchy-saturated porous media, J. Acoust. Soc. Am., 110(2), 682-

542   694, doi:10.1121/1.1381021, 2001.

543   Jo, C.H., Shin, C.S., and Suh, J.H.: An optimal 9-point, finite-difference, frequency-space, 2-D scalar wave extrapolator,

544   Geophysics, 61, 529-537, doi:10.1190/1.1443979, 1996.

545   Khokhlov, N., Favorskaya, A., Stetsyuk, V., Mitskovets, I.: Grid-characteristic method using Chimera meshes for simulation

546   of elastic waves scattering on geological fractured zones, J. Comput. Phys., 446, 110637, doi:10.1016/j.jcp.2021.110637,

547   2021.

548   Krzikalla, F. and Müller T. M.: Anisotropic P-SV-wave dispersion and attenuation due to inter-layer flow in thinly layered

549   porous rocks, Geophysics, 76, WA135-WA145, doi:10.1190/1.3555077, 2011.

550   Kudarova, A. M., Karel, V. D., and Guy D.: An effective anisotropic poroelastic model for elastic wave propagation in finely

551   layered media, Geophysics, 81, 175-188, doi:10.1190/geo2015-0362.1, 2016.

552   Liu E. R., Hudson J. A., and Pointer T.: Equivalent medium representation of fractured rock, J. Geophys. Res., 105, 2981-3000,

553   doi:10.1029/1999JB900306, 2000.

554   Liu, X., Greenhalgh, S., Zhou, B., and Greenhalgh, M.: Frequency-domain seismic wave modelling in heterogeneous porous

555   media using the mixed-grid finite-difference method, Geophys J Int., 216, 34-54, doi:10.1093/gji/ggy410, 2018.

556   Müller, T. M., Stewart J. T., and Wenzlau, F.: Velocity-saturation relation for partially saturated rocks with fractal pore fluid

557   distribution, Geophys. Res. Lett., 35, L09306, doi:10.1029/2007GL033074, 2008.

558   Nakagawa, S. and Schoenberg M. A.: Poroelastic modeling of seismic boundary conditions across a fracture, J. Acoust. Soc.

559   Am., 122, 831-847, doi:10.1121/1.2747206, 2007.

560   Norris, A. N.: Low-frequency dispersion and attenuation in partially saturated rocks, J. Acoust. Soc. Am., 94, 359-370,

561   doi:10.1121/1.407101, 1993.

562   Oelke, A., Alexandrov, D., Abakumov, I., Glubokovskikh, S., Shigapov, R., Krüger, O. S., Kashtan, B., Troyan, V., and Shapiro,

563   S. A.: Seismic reflectivity of hydraulic fractures approximated by thin fluid layers, Geophysics, 78, 79-87,

564   doi:10.1190/geo2012-0269.1, 2013

565   Operto, S., Virieux, J., Ribodetti, A., and Anderson J. E.: Finite-difference frequency-domain modeling of viscoacoustic wave

566   propagation in 2D tilted transversely isotropic (TTI) media, Geophysics, 74, 75-95, doi:10.1190/1.3157243, 2009.

567   Rubino, J. G., Müller T. M., Guarracino L., Milani M., and Holliger K.: Seismoacoustic signatures of fracture connectivity, J.

568   Geophys. Res. Solid Earth., 119, 2252-2271, doi:10.1002/2013JB010567, 2014.

569   Rubino, J. G., Castromán G. A., Müller T. M., Monachesi L. B., Zyserman F. I., and Holliger K.: Including poroelastic effects

570   in the linear slip theory, Geophysics, 80, A51-A56, doi:10.1190/geo2014-0409.1, 2015.

571   Sayers, C. M. and Kachanov M.: Microcrack-induced elastic wave anisotropy of brittle rocks, J. Geophys. Res., 100, 4149-

572   4156, doi:10.1029/94JB03134, 1995.

573   Schoenberg, M. A.: Elastic wave behavior across linear slip interfaces, J. Acoust. Soc. Am., 68, 1516-1521,

574   doi:10.1121/1.385077, 1980.

575   White, J. E., Mikhahaylova, N. G., and Lyakhovistsky, F. M.: Low-frequency seismic waves in fluid-saturated layered rocks,

576   Izv., Acad. Sci., USSR, Phys. Solid Earth., 11, 654-659, doi:10.1121/1.1995164, 1975.

577   Zhang, J. F.: Elastic wave modeling in fractured media with an explicit approach, Geophysics, 70, 75-85,

578   doi:10.1190/1.2073886, 2005.